Carbonate Detection With SuperCam in Igneous Rocks on the Floor of Jezero Crater, Mars

E. Clavé, K. Benzerara, P.-y. Meslin, O. Forni, C. Royer, L. Mandon, P. Beck, C. Quantin-Nataf, O. Beyssac, A. Cousin, et al.

▶ **To cite this version:**

E. Clavé, K. Benzerara, P.-y. Meslin, O. Forni, C. Royer, et al.. Carbonate Detection With SuperCam in Igneous Rocks on the Floor of Jezero Crater, Mars. Journal of Geophysical Research. Planets, 2023, The MARS Perseverance Rover Jezero Crater Floor Campaign, 128 (6), 10.1029/2022JE007463 . hal-04232122

HAL Id: hal-04232122
https://hal.science/hal-04232122

Submitted on 1 Nov 2023

HAL is a multi-disciplinary open access archive for the deposit and dissemination of scientific research documents, whether they are published or not. The documents may come from teaching and research institutions in France or abroad, or from public or private research centers.

L'archive ouverte pluridisciplinaire **HAL**, est destinée au dépôt et à la diffusion de documents scientifiques de niveau recherche, publiés ou non, émanant des établissements d'enseignement et de recherche français ou étrangers, des laboratoires publics ou privés.

JGR Planets

RESEARCH ARTICLE
10.1029/2022JE007463

Special Section:
The Mars Perseverance Rover Jezero Crater Floor Campaign

Carbonate Detection With SuperCam in Igneous Rocks on the Floor of Jezero Crater, Mars

E. Clavé[1], K. Benzerara[2], P.-Y. Meslin[3], O. Forni[3], C. Royer[4], L. Mandon[4], P. Beck[5], C. Quantin-Nataf[6], O. Beyssac[2], A. Cousin[3], B. Bousquet[1], R. C. Wiens[7], S. Maurice[3], E. Dehouck[6], S. Schröder[8], O. Gasnault[3], N. Mangold[9], G. Dromart[10], T. Bosak[11], S. Bernard[2], A. Udry[12], R. B. Anderson[13], G. Arana[14], A. J. Brown[15], K. Castro[14], S. M. Clegg[16], E. Cloutis[17], A. G. Fairén[18,19], D. T. Flannery[20], P. J. Gasda[16], J. R. Johnson[21], J. Lasue[3], G. Lopez-Reyes[22], J. M. Madariaga[14], J. A. Manrique[22], S. Le Mouélic[9], J. I. Núñez[21], A. M. Ollila[16], P. Pilleri[3], C. Pilorget[23], P. Pinet[3], F. Poulet[23], M. Veneranda[22], Z. U. Wolf[17], and the SuperCam team[24]

[1]CELIA, Université de Bordeaux, CNRS, CEA, Bordeaux, France, [2]Institut de Minéralogie, Physique des Matériaux et Cosmochimie, CNRS UMR, Sorbonne Université, Muséum National d'Histoire Naturelle, Paris, France, [3]IRAP, Université de Toulouse, CNRS, UPS, CNES, Toulouse, France, [4]LESIA, Observatoire de Paris, Université PSL, CNRS, Sorbonne Université, Université de Paris, Meudon, France, [5]Institut de Planétologie et d'Astrophysique de Grenoble, Université Grenoble Alpes, CNRS CNES, Grenoble, France, [6]Univ Lyon, UCBL, ENSL, UJM, CNRS, LGL-TPE, Villeurbanne, France, [7]Earth, Atmospheric, and Planetary Sciences, Purdue University, West Lafayette, IN, USA, [8]DLR Institute of Optical Sensor Systems, Berlin, Germany, [9]LPG, CNRS, Nantes Université, Université Angers, Nantes, France, [10]Laboratoire de Géologie de Lyon, Université de Lyon, Lyon, France, [11]Department of Earth, Atmospheric and Planetary Sciences, Massachusetts Institute of Technology, Cambridge, MA, USA, [12]Department of Geoscience, University of Nevada Las Vegas, Las Vegas, NV, USA, [13]U. S. Geological Survey Astrogeology Science Center, Flagstaff, AZ, USA, [14]Department of Analytical Chemistry, University of the Basque Country UPV/EHU, Leioa, Spain, [15]Plancius Research, Severna Park, MD, USA, [16]Los Alamos National Laboratory, Los Alamos, NM, USA, [17]C-TAPE, University of Winnipeg, Winnipeg, MB, Canada, [18]Centro de Astrobiología (CSIC-INTA), Madrid, Spain, [19]Department of Astronomy, Cornell University, Ithaca, NY, USA, [20]School of Earth and Atmospheric Sciences, Queensland University of Technology, Brisbane, QLD, Australia, [21]Johns Hopkins University Applied Physics Laboratory, Laurel, MD, USA, [22]Research group ERICA, Universidad de Valladolid (UVa), Valladolid, Spain, [23]IAS, Université Paris-Saclay, Orsay Cedex, France, [24]See Supporting Information S1

Key Points:

- Carbonates are detected along Perseverance's traverse in Jezero Crater with SuperCam using laser-induced breakdown spectroscopy, IR and Raman spectroscopy
- Carbonate abundance is low overall, consistent with the weak carbonate signatures observed from orbit in the explored units
- The detected carbonates have variable compositions within the magnesite-siderite series, and likely reflect multiple alteration episodes

Supporting Information:

Supporting Information may be found in the online version of this article.

Correspondence to:

E. Clavé,
elise.clave@u-bordeaux.fr

Citation:

Clavé, E., Benzerara, K., Meslin, P.-Y., Forni, O., Royer, C., Mandon, L., et al. (2023). Carbonate detection with SuperCam in igneous rocks on the floor of Jezero Crater, Mars. *Journal of Geophysical Research: Planets*, *128*, e2022JE007463. https://doi.org/10.1029/2022JE007463

Received 8 JUL 2022
Accepted 7 DEC 2022

© 2022. American Geophysical Union. All Rights Reserved.

Abstract

Perseverance explored two geological units on the floor of Jezero Crater over the first 420 Martian days of the Mars2020 mission. These units, the Máaz and Séítah formations, are interpreted to be igneous in origin, with traces of alteration. We report the detection of carbonate phases along the rover traverse based on laser-induced breakdown spectroscopy (LIBS), infrared reflectance spectroscopy (IRS), and time-resolved Raman (TRR) spectroscopy by the SuperCam instrument. Carbonates are identified through direct detection of vibrational modes of CO_3 functional groups (IRS and TRR), major oxides content, and ratios of C and O signal intensities (LIBS). In Séítah, the carbonates are consistent with magnesite-siderite solid solutions (Mg# of 0.42–0.70) with low calcium contents (<5 wt.% CaO). They are detected together with olivine in IRS and TRR spectra. LIBS and IRS also indicate a spatial association of the carbonates with clays. Carbonates in Máaz are detected in fewer points, as: (a) siderite (Mg# as low as 0.03); (b) carbonate-containing coatings, enriched in Mg (Mg# ~0.82) and spatially associated with different salts. Overall, using conservative criteria, carbonate detections are rare in LIBS (~30/2,000 points), IRS (~15/2,000 points), and TRR (1/150 points) data. This is best explained by (a) a low carbonate content overall, (b) small carbonate grains mixed with other phases, (c) intrinsic complexity of in situ measurements. This is consistent with orbital observations of Jezero crater, and similar to compositions of carbonates previously reported in Martian meteorites. This suggests a limited carbonation of Jezero rocks by locally equilibrated fluids.

Plain Language Summary

Carbonates are mineral phases that generally form by alteration of primary, magmatic minerals. This alteration process may occur under a variety of environmental conditions, which affect the resulting carbonate phase: its abundance, composition, spatial distribution and the mineral phases it is associated with. Consequently, carbonates keep track of the environmental conditions under which they formed, and in particular, the amount of CO_2 and liquid water involved in their formation. Understanding the history of both water and CO_2 on Mars is critical to better understand the evolution of the red planet and its atmosphere, but also the origin of the water on Earth, and possibly the origin of life. Since the beginning of the Mars2020 mission in Jezero Crater, the SuperCam instrument has analyzed more than 200 rocks of the crater

floor, and detected carbonates along Perseverance's traverse. Carbonates are found in low amounts, and are therefore complex to identify; we use SuperCam's combination of investigation techniques and a specifically developed methodology to strengthen the identification of carbonate phases and their characterization. Even though Jezero crater hosted a lake billions of years ago, the detected carbonates appear to have formed in smaller amounts of water, after the lake had disappeared.

1. Introduction

Martian carbonate mineral phases have received particular attention due to their high scientific value. First, they may compose a significant reservoir of carbon on Mars in addition to the regolith (Zent & Quinn, 1995) and ice caps (Phillips et al., 2011), which have altogether been exchanging C with the atmosphere over geological time and therefore impacted the Martian climate (Jakosky & Edwards, 2018; Manning et al., 2006). The loss of some C to space may explain the low modern C inventory (Jakosky et al., 2018; Lammer et al., 2013). However, the numerous traces of past liquid water activity at the surface of Mars in the first billion years require either a CO_2-dominated atmosphere, denser than at present and providing a continuous greenhouse effect (Kite et al., 2021), or that overall icy conditions transiently warmed just enough to allow liquid water to episodically shape the surface (Fairén, 2010; Fairén et al., 2009; Kite et al., 2017; Ramirez & Craddock, 2018; Wordsworth et al., 2018). Assuming the presence of such a thicker, CO_2-rich atmosphere, it should have led to the formation of carbonates following water-rock interactions. This is why the apparent scarcity of carbonates at the surface of Mars has been intriguing, resulting in a "missing carbon" problem (Bibring et al., 2005; Morris et al., 2010). Overall, assessing the abundance of carbonates on Mars is key to achieving a better inventory of the C budget on Mars, which is itself crucial to better understanding the evolution of environmental conditions at the surface of this planet. Second, carbonate phases record direct information about the chemical composition, pH, and temperature of the past fluids in which they precipitated, which can be decrypted based on a suite of textural and geochemical analyses (e.g., Bridges et al., 2019; Fairén et al., 2004; Niles et al., 2013). Last, carbonates can host traces of life as shown by multiple terrestrial examples, and can thus provide valuable targets in the search for past life on Mars (Benzerara et al., 2018; Bosak et al., 2021; Farmer & Des Marais, 1999).

Martian carbonates have been detected multiple times based on different records (Bridges et al., 2019). One consists of several Martian meteorites with two different types of characteristics: (a) carbonates in the orthopyroxenite Allan Hills (ALH) 84001 are Noachian, formed 3.9–4.0 Ga ago and composed of zoned calcite, dolomite-ankerite, and magnesite-siderite (Harvey & McSween, 1996; Treiman, 2021; Valley et al., 1997). These chemically diverse pools of carbonates formed in different precipitation events, at low temperatures (10°C–22°C) (Halevy et al., 2011; Shaheen et al., 2015). Some of these carbonates contain magnetites, which were considered as likely biogenic by some authors (Jimenez-Lopez et al., 2012; Thomas-Keprta et al., 2009), but alternatively interpreted as abiotic products of shock metamorphism (Golden et al., 2004). (b) By contrast, carbonates in nakhlites belong to the siderite-magnesite solid solution (e.g., Bridges et al., 2019). They are located in veins, mixed with phyllosilicates and formed less than 670 Ma ago, possibly under hydrothermal conditions created by some impact events. It should also be noted that some Ca-carbonates found in Martian meteorites are interpreted as terrestrial contaminants (García-Florentino et al., 2021; Shaheen et al., 2015).

Martian carbonates have also been detected from orbit by visible and infrared (VISIR) spectrometers such as the Compact Reconnaissance Imaging Spectrometer for Mars (CRISM) on the Mars Reconnaissance Orbiter (MRO), (e.g., Ehlmann et al., 2008; Goudge et al., 2015; Horgan et al., 2020). The majority of carbonates have been detected near Isidis Basin, including in the Jezero crater (e.g., Ehlmann et al., 2008; Horgan et al., 2020), although carbonates have also been detected in other places on Mars where deposits have been excavated by impact craters (Wray et al., 2016). They have been interpreted to mostly contain Mg and Fe in various proportions (Brown et al., 2020; Ehlmann et al., 2008; Tarnas et al., 2021) and often associated with clay minerals (Wray et al., 2016). Low levels (<10%) of Mg-carbonates widespread across the Martian surface were also reported from analysis of data acquired by the Planetary Fourier Spectrometer on board the Mars Express spacecraft (Palomba et al., 2009).

Finally, several detections of Martian carbonates have been achieved in situ, at the surface of Mars. For example, Fe-Mg carbonates were inferred in the Comanche outcrop of the Columbia Hills in Gusev crater by *Spirit's* Alpha Particle X-ray Spectrometer and Miniature Thermal Emission Spectrometer (Mini-TES) instruments (Morris et al., 2010). At this location, olivine-bearing basalts were estimated to be Hesperian in age, and carbonate phases

were estimated to represent ~26% of the total outcrop. At around the same time, the Phoenix lander detected small amounts of Ca-carbonates in Martian polar soil using the Thermal and Evolved-Gas Analyzer (TEGA) instrument (Boynton et al., 2009). Last, Fe- and/or Mg-carbonates were detected at the percent level in lacustrine and eolian deposits in Gale crater by *Curiosity*'s Sample Analysis at Mars (SAM) and Chemistry and Mineralogy (CheMin) instruments (Bristow et al., 2021; Sutter et al., 2017; Thorpe et al., 2021).

The Mars 2020 mission is strongly focused on the topic of carbonates at the surface of Mars, with the additional objective to prepare the return of samples to the Earth (International MSR Objectives and Samples Team (iMOST) et al., 2019). This will offer a unique opportunity to exhaustively characterize these carbonates in pristine samples, better assess past environmental conditions at the surface of Mars and search for traces of past life. The detection of carbonate mineral phases from orbit has been critical in supporting the choice of the Jezero crater as a landing site for the Mars 2020 mission. Indeed, this Noachian-aged crater lies within the largest carbonate-rich unit detected on Mars from orbit (Brown et al., 2020; Ehlmann et al., 2008; Goudge et al., 2015; Horgan et al., 2020; Mandon et al., 2020; Tarnas et al., 2021). Carbonates in Jezero are found in diverse geological units, such as the olivine-carbonate unit which extends to the whole Nili Fossae region, or the "Marginal carbonates" unit (Horgan et al., 2020). Carbonates in these diverse units may have formed through different geological processes, with those in the "Marginal carbonates" unit possibly having formed as authigenic lacustrine phases (Horgan et al., 2020). Overall, this outlines the importance to characterize these phases in more detail from the surface.

The *Perseverance* rover landed in Jezero Crater on 18 February 2021, and spent the first ~420 Martian days (sols) exploring the crater floor before investigating a river delta formation (Mangold et al., 2021), which is a prime target of the mission. In particular, two distinct geological formations were investigated (Farley et al., 2022; Wiens et al., 2022). The Máaz formation (fm) was explored over sols 1-201, and again from sol 342 to 416. It corresponds to the crater floor fractured rough (Cf-fr) as mapped previously (Stack et al., 2020). The Máaz fm consists of apparent basaltic to basaltic-andesitic lava and possible pyroclastic flows mostly containing multiple pyroxenes (Fe-rich augite, pigeonite, and clino-enstatite) as well as plagioclase, and likely originating from a single parental magma (Udry et al., 2022). The Séítah fm (crater floor fractured—cf-f1 in Stack et al., 2020) was explored over sols 202–342, although the first Seitah rocks were analyzed on sols 173–178, while driving along the Seitah-Maaz contact. After an intensive drive campaign from sols 380 to 415, Perseverance encountered Séítah-like materials (cf-f2 in Stack et al., 2020) again in front of the delta on sols 416–420. These materials are characterized by strong olivine IR signatures in the orbital (Brown et al., 2020; Horgan et al., 2020; Tarnas et al., 2021) and ground data (Beyssac et al., 2023; Farley et al., 2022; Liu et al., 2022; Wiens et al., 2022). These signatures are similar to those in a regional olivine-carbonate unit, whose origin remains debated, (e.g., Mandon et al., 2020). The Séítah fm underlies the Máaz formation and is another igneous formation seemingly genetically unrelated to the Máaz fm (Udry et al., 2022) and interpreted as an olivine cumulate (Beyssac et al., 2023; Farley et al., 2022; Liu et al., 2022; Wiens et al., 2022). Within the Séítah fm, a distinct member, called the Content member, was identified (Horgan et al., 2022; Núñez et al., 2022); it differs from Séítah rocks by its morphology—the rocks are pitted—and its composition—less primitive than Séítah rocks and actually close to the composition of Máaz rocks (Wiens et al., 2022). Although primary mineralogy is generally well preserved (Beyssac et al., 2023; Udry et al., 2022), secondary phases are found in both Máaz and Séítah (e.g., Mandon et al., 2022; Meslin et al., 2022; Farley et al., 2022; Tice et al., 2022; Wiens et al., 2022).

The “Marginal carbonates” unit, although key when talking about carbonates in Jezero Crater, has not been investigated by Perseverance yet and will therefore not be discussed in this study.

Perseverance is equipped with seven different analytical instruments, including SuperCam, a mast-based multi-technique instrument combining several imaging and spectroscopy techniques (Maurice et al., 2021; Wiens et al., 2021). SuperCam characterizes the chemistry, mineralogy, and texture of rocks and soils located nominally within a distance of 2–7 m from the rover—although targets were analyzed with laser-induced breakdown spectroscopy (LIBS) as far as ~10 m away—at stops along the traverse. Here, we analyze these data to assess the presence of carbonates, their spatial distribution, their chemical composition, and the nature of the mineral phases with which they are associated. We use these data to investigate the carbonate formation processes that may have occurred in Jezero.

2. Materials and Methods

2.1. The SuperCam Instrument

As one of the remote sensing instruments of *Perseverance's* payload, SuperCam enables the analysis of a large number of geologic target. along the rover traverse, thus providing significant statistics, as well as a broad overview of the distribution of different mineral species and their composition. SuperCam can perform four types of spectroscopy: LIBS, time-resolved Raman (TRR), time-resolved luminescence (TRL), and visible and infrared reflectance (VISIR) spectroscopy. Moreover, SuperCam is equipped with a remote micro-imager (RMI) providing context color images, and a microphone to assess physical parameters of the targets. TRL and acoustic data were not used in the present study, and therefore will not be further described. Details about the instrument and the associated techniques are provided elsewhere (Maurice et al., 2021; Wiens et al., 2021).

2.1.1. Principles and Characteristics of the Spectroscopy and Imaging Tools Provided by SuperCam

LIBS and TRR are laser-based spectroscopy techniques. The pulsed Nd-YAG laser used for LIBS at 1,064 nm is positioned at the top of the mast of Perseverance. The same laser can also be operate at 532 nm through the use of a second-harmonic generator for TRR. The laser pulse duration is 3–4 ns and the repetition rate is 3 Hz for LIBS and 10 Hz for TRR. For both techniques, the emitted/scattered light is collected by a 110 mm diameter telescope and transferred to the SuperCam spectrometers through a bundle of optical fibers. SuperCam is equipped with three spectrometers covering complementary spectral ranges: 243.7–345.0 nm (UV), 379.0–465.0 nm (VIO), and 532.0–858.8 nm (VIS). The spectrometers covering the UV and VIO ranges are Czerny-Turner, whereas the third one is a transmission time-gated spectrometer equipped with an intensified CCD camera that enables time-gated observations.

The three spectroscopy techniques and RMI images are co-aligned, enabling a selected point on a Martian target to be characterized by LIBS for chemistry, as well as TRR and VISIR for mineralogy, although the analytical footprints are of different sizes (details below).

For LIBS, a small amount of material is ablated from the target and ionized, thus creating a plasma. The transient plasma emission is at the origin of the LIBS spectrum. In particular, narrow emission lines—characteristic of the ions and atoms present in the plasma—are used to infer the elemental composition of the ablated target. LIBS is mostly sensitive to major elements—such as Si, Ti, Al, Fe, Mg, Ca, Na, and K. Many additional elements can also be detected, including Mn, H, and C (Maurice et al., 2021). In the context of Martian exploration, LIBS enables stand-off analyses of both regolith and rocks. Analyses take only a few minutes per target. LIBS has been used successfully for Martian exploration since 2012, with the ChemCam instrument, aboard Curiosity (Maurice et al., 2012, 2016; Wiens et al., 2012). SuperCam LIBS laser spot size—and therefore analyzed area—is ∼0.35–0.55 mm in diameter.

Raman scattering provides information about the vibrational and rotational frequency of molecular bonds, allowing the identification of molecules, and in some cases, mineral phases based on lattice vibration (Gardiner & Graves, 1989). On SuperCam, as opposed to the focused infrared laser beam used for LIBS, TRR is operated with the 1-cm-diameter collimated green laser beam, co-aligned with the telescope-spectrometer system; the field-of-view of 0.7 mrad for targets up to 7 m is given by the collection path. TRR is analyzed by the VIS spectrometer, synchronized with the laser pulse.

VISIR is based on the reflection of sunlight onto the target surface. VISIR probes the frequencies of molecule bond vibrations, which are characteristic of the molecules. This information can ultimately be interpreted in terms of mineralogical composition of the targets (e.g., J. L. Bishop, 2019). On SuperCam, the spectrum of reflected light in the 1.3–2.6 μm range corresponding to infrared spectroscopy (IRS) is acquired by an acousto-optic tunable filter (AOTF) spectrometer (Fouchet et al., 2022). The analytical footprint of IRS has a diameter of ∼1.15 mrad. As opposed to LIBS and TRR, IRS does not involve laser excitation and can thus be applied to targets located up to several kilometers away from the rover. Since the diagnostic signatures of carbonates are in the infrared range, we focus mostly on IRS in this study, rather than VISIR in general.

The RMI provides high-resolution images, documenting the textural context for the spectroscopy analyses, as well as standalone detailed observations of remote outcrops. The field of view of the RMI is 18.8 mrad with an optical resolution of ∼0.080 mrad (Gasnault et al., 2012), while details almost twice as small can be seen under optimal conditions.

2.1.2. Operation of the Instrument

SuperCam probes targets with an analytical footprint of 0.35–0.55 mm for LIBS, 1.4–4.9 mm for TRR and 2.3–8.1 mm for IRS for targets located 2–7 m away (see Figure 50 in Maurice et al., 2021). To get representative information from heterogeneous rocks, spectra are typically acquired in series of 5 or 10 points in lines, or 3×3 grids, referred to as rasters. Two or three RMI images are usually acquired to provide context and textural information on the target.

On each point, one or several of SuperCam spectroscopy techniques can be used. LIBS generally comes first, because the shock-wave induced by the plasma expansion cleans the dust from the target's surface, reducing the contribution of dust to the VISIR and/or TRR spectra acquired afterward (Maurice et al., 2021; Sharma et al., 2007). On each point, 30 laser shots are generally fired for LIBS. All spectra are returned, but the first five shots, which often sample the dust (Lasue et al., 2018; Maurice et al., 2016; Meslin et al., 2013), are automatically removed on Earth before averaging the shot-to-shot LIBS spectra.

For Raman observations, the gate width is set at 100 ns to record the Raman signal and reduce the influence of interfering signals, such as mineral luminescence or daylight. Since Raman scattering is a low-efficiency process, Raman analyses require the accumulation of signal over multiple laser shots to enable the Raman signal to build up above noise level. A Raman observation with SuperCam at the surface of Mars typically uses 100–400 laser shots at each point analyzed.

Depending on the time of day and temperature of the instrument, IRS preset exposure times are 30–205 ms per spectral channel, and 256 spectral channels are acquired over the 1.3–2.6 μm range.

2.2. Onboard Calibration Targets

The SuperCam calibration targets (SCCTs) are a series of samples of known composition located at the back of the Perseverance rover, to monitor the performance of each technique and the processing methods applied to SuperCam Martian data (Cousin et al., 2022; Manrique et al., 2020).

The SCCTs include a calcite target that is particularly useful in the present study. The chemical composition of the powdered reference calcite used to create the target was characterized with inductively coupled plasma mass spectrometry (ICP-MS) and electron microprobe (Cousin et al., 2022). The mineral sample was powdered and flash sintered to obtain a cohesive pellet, in order to meet the thermal and mechanical requirements of the mission (Montagnac et al., 2018). TRR and VISIR analyses performed on Earth after this processing showed the expected calcite signatures (Cousin et al., 2022; Madariaga et al., 2022).

Two other SCCTs were originally designed as carbonate-rich targets—a siderite and an ankerite. However, laboratory analyses of these targets (including TRR and VISIR) after the sintering process showed that they had been altered and could no longer be considered as reference carbonates (Cousin et al., 2022; Montagnac et al., 2018). As a consequence, these two SCCTs are not used in the present study.

2.3. Data Processing

2.3.1. LIBS

2.3.1.1. Pre-Processing

All LIBS spectra are submitted to a series of pre-processing steps, as part of a standardized pipeline. These different pre-processing steps are presented elsewhere (R. B. Anderson et al., 2021).

Normalization is applied as an additional step to correct for variations of laser-target coupling and distance effects. In most cases, each portion of a spectrum is divided by the total area of the spectrum acquired in the corresponding spectral range. However, to study minor elements with few emission lines, this normalization may introduce biases related to the emission of major elements, especially those with a high density of emission lines. Therefore, the analysis of the C signal is based on the comparison of the C and O intensities using the intensity of the O I triplet at 777 nm, extracted from unnormalized spectra (Beck et al., 2017; Gasnault et al., 2012; Wiens et al., 2012).

LIBS spectra exhibiting total emission $<10^{14}$ photons/pulse/sr/mm^2 over the collected spectral range are excluded, because of poor laser-target coupling. Moreover, we work only with targets analyzed at distances smaller than 6.5 m, to reduce uncertainties related to non-linear physical effects with laser irradiance varying with the distance. Points with a bad focus were excluded manually from the data set. Since the laser-target coupling is different on fine-grained materials, resulting in varying plasma emissions, we also exclude points on fine-grained regolith or core/abrasion tailings.

2.3.1.2. Major-Element Oxides Composition (MOC), Quantification Models

To quantify the major-element oxides composition (MOC) from the Martian LIBS spectra, we use a series of multivariate models, trained on SuperCam laboratory LIBS spectra and presented elsewhere (R. B. Anderson et al., 2021). Applying these models to the Martian data gives contents in oxides SiO_2, TiO_2, Al_2O_3, FeOt, MgO, CaO, Na_2O, and K_2O for each point analyzed with LIBS.

The precision of the quantification is better than its accuracy (Table S1 in Supporting Information S1) (R. B. Anderson et al., 2021). As a consequence, the MOC data can be used with confidence to compare the Martian observations with each other and with SCCTs, especially when the distance to the target is between 2 and 4 m.

As a first approach in the carbonate detection method, we plot molar compositions derived from the MOC data in a Si + Al/Fe + Mg/Ca + Na + K ternary diagram. In this representation, carbonate-rich points are expected to plot far from the Al + Si apex. We expect their SiO_2 content to be smaller than 30 wt.%, that is the SiO_2 content in fayalite—the silicate phase with the lowest degree of polymerization, hence the lowest SiO_2 content. Moreover, the total of the MOC for carbonate-rich points is expected to be relatively low, since CO_3 content is not included. It can be noted that these criteria are (a) also met by other mineral phases such as oxi-/hydroxides (Fe, Mn, Ti, …), sulfates, and possibly other salts such as phosphates, perchlorates (see Meslin et al., 2022); (b) relative, and dependent of the uncertainties on the MOC data; (c) restrictive for detecting carbonates and will only help to identify points with a very high carbonate content.

Additionally, we expect Al_2O_3, Na_2O, and K_2O to be low (indicative thresholds around respectively 5, 2.5, and 1 wt.%) and CaO, FeO, and/or MgO to be relatively high in carbonate-rich points (CaO + FeO + MgO > 40 wt.%). We do not set strict thresholds on these elements, but take these values into account to assess the reliability of potential carbonate detections.

From the MOC data, we compute the Mg# defined as the molar Mg content divided by the sum of the molar Mg and Fe contents. Comparing the Mg# values obtained from all SCCT observations with LIBS on Mars versus the values measured by ICPMS on Earth, we observe a good 1:1 correlation, except for the calcite and orthoclase targets, which both have very low Mg and Fe contents, resulting in higher uncertainties when ratioed (slope of 0.95 and R^2 of 0.97 without the calcite and orthoclase).

The multiple spectra produced by a number of laser shots on a single observation point are usually averaged to produce a single composition, as presented above. Additionally, the spectra corresponding to single laser shots show the evolution of the signal with depth, as the laser digs through tens of micrometers into the target, potentially highlighting the presence of coatings or mineral mixtures (e.g., Lanza et al., 2015). In the context of this study, we observe single-shot—also called shot-to-shot—data to investigate mixtures of carbonate with other mineral phases; different shots sometimes document varying proportions of mixed phases and help constraining the composition of the carbonates versus that of the phases in mixture, as well as the depth at which carbonates are generally detected (directly at the surface or at a depth of a few tens of micrometers).

The quantification models presented are originally trained and designed to be used on averaged spectra. They can be used to estimate composition from single shot spectra, but the uncertainties are expected to be larger, because of the reduced signal-to-noise ratio (SNR) as well as the variation of laser-target coupling and plasma confinement as the ablation digs into the sample. Consequently, shot-to-shot data should be interpreted with caution, considering all shots from one profile together rather than individual shots separately.

2.3.1.3. Direct Detection and Characterization of C

Carbonate analyses can yield MOC values similar to other phases such as oxides, oxyhydroxides, phosphates, or sulfates. To distinguish among these possible phases, we also rely on the direct detection of minor elements (e.g., Meslin et al., 2022). In this study we focus on carbon, using C emission lines in the LIBS spectra (D. E.

Anderson et al., 2017; Ollila et al., 2011). We use carbon emission lines at 678 and 723 nm, because these lines were shown to be better correlated with the carbon content of the target compared to other lines (D. E. Anderson et al., 2017), as well as the O signature at 777 nm; details on the fitted emission lines are given in Text S1 in Supporting Information S1.

However, the breakdown of atmospheric CO_2 from the Martian atmosphere in the plasma results in systematic C detection in Martian LIBS spectra (Dequaire et al., 2017; Schröder et al., 2019; Wiens et al., 2012). Identifying carbonates requires that we discriminate atmospheric carbon from carbon within rock/regolith targets. To do so, we need to account for the effects of two physical parameters: the laser-target coupling efficiency, and the laser irradiance on the target. Further details and illustration about this are provided in Text S2 and Figures S1–S4 in Supporting Information S1.

First, we use the O emission as an internal standard to correct for the coupling efficiency; previous work has shown that in carbon-free samples analyzed at a given distance, the contributions of atmospheric carbon and oxygen result in correlated C and O signals, whose intensities depend on the laser-target coupling efficiency (Beck et al., 2017; Gasnault et al., 2012; Wiens et al., 2012). The oxygen content of the sample has only a second-order influence on the oxygen line intensity. It has been shown that, at a given distance, targets containing carbonates show a higher C signal, and a higher carbon-to-oxygen ratio. If we suppose that the majority of the points analyzed on Mars have low C content, we can characterize the atmospheric C-to-O ratio for a given distance by fitting the C versus O intensities with a linear trend (illustrated in Figure S1 in Supporting Information S1). We can thus define a proxy for non-atmospheric carbon signal as the horizontal distance (ΔC) of a point to this atmospheric trend in the biplot of the C versus O intensities; we normalize this distance to the standard deviation of the points around the atmospheric trend.

Since the laser irradiance varies with distance, we define different distance bins, and work only with targets analyzed at comparable distances. We define a set of distance bins such that each target belongs to 5 to 21 bins and apply the process described above to each bin; we then combine the different bins to finally obtain a C score for each point, corrected for both coupling and distance effects.

We then use Student's distribution to set a threshold for non-atmospheric carbon detection based on this C score: we use a threshold value of 1.28, which, based on the Gaussian distribution of a large set of points, corresponds to a 10% risk of false positives. We select points with a C score higher than this threshold value and then use the MOC to confirm the presence of carbonates among these points, using the criteria detailed in Section 2.3.1.2.

2.3.2. Time-Resolved Raman (TRR) Spectroscopy

The pre-processing of Raman spectra starts with spikes removal through a sigma-clipping algorithm. The following steps are similar to those used for LIBS data: dark subtraction, stitching together adjacent spectral ranges, denoising, wavenumber calibration, and instrument response function (IRF, Legett et al., 2022) correction (Algermissen & Padgett, 2021).

To characterize Raman features, peaks are extracted with Mexican Hat Wavelet filters of various widths (Guo et al., 2008). For each peak, the SNR is computed by dividing the signal by the standard deviation of the background, which is estimated with the method described for LIBS in R. B. Anderson et al. (2021). Peaks detected at similar positions with all filters are compared and the ones with the highest SNR ratio are retained.

For interpretation of the data, only peaks with a SNR higher than 50 are considered. Moreover, to confirm detection and discriminate Raman peaks from random spikes, we ascertain that the feature is visible in more than one spectrum acquired at a given point.

2.3.3. Infrared Spectroscopy (IRS)

SuperCam IRS calibration and data acquired over the first year of the M2020 mission are presented in depth elsewhere (Mandon et al., 2022; Royer et al., 2022), including the processing of the spectra, as well as the mineral signatures observed so far.

We characterize the depth of the carbonate 2.3- and 2.5-μm absorption bands using the methodology presented elsewhere (Viviano-Beck et al., 2014). For each band, we define three key wavelength values: right and left shoulders, and a center. We use the shoulders to compute a local baseline and then compute the depth of the band, at the center, with respect to this baseline. For the 2.3-μm band, we place the shoulders at 2.24 and 2.36 μm,

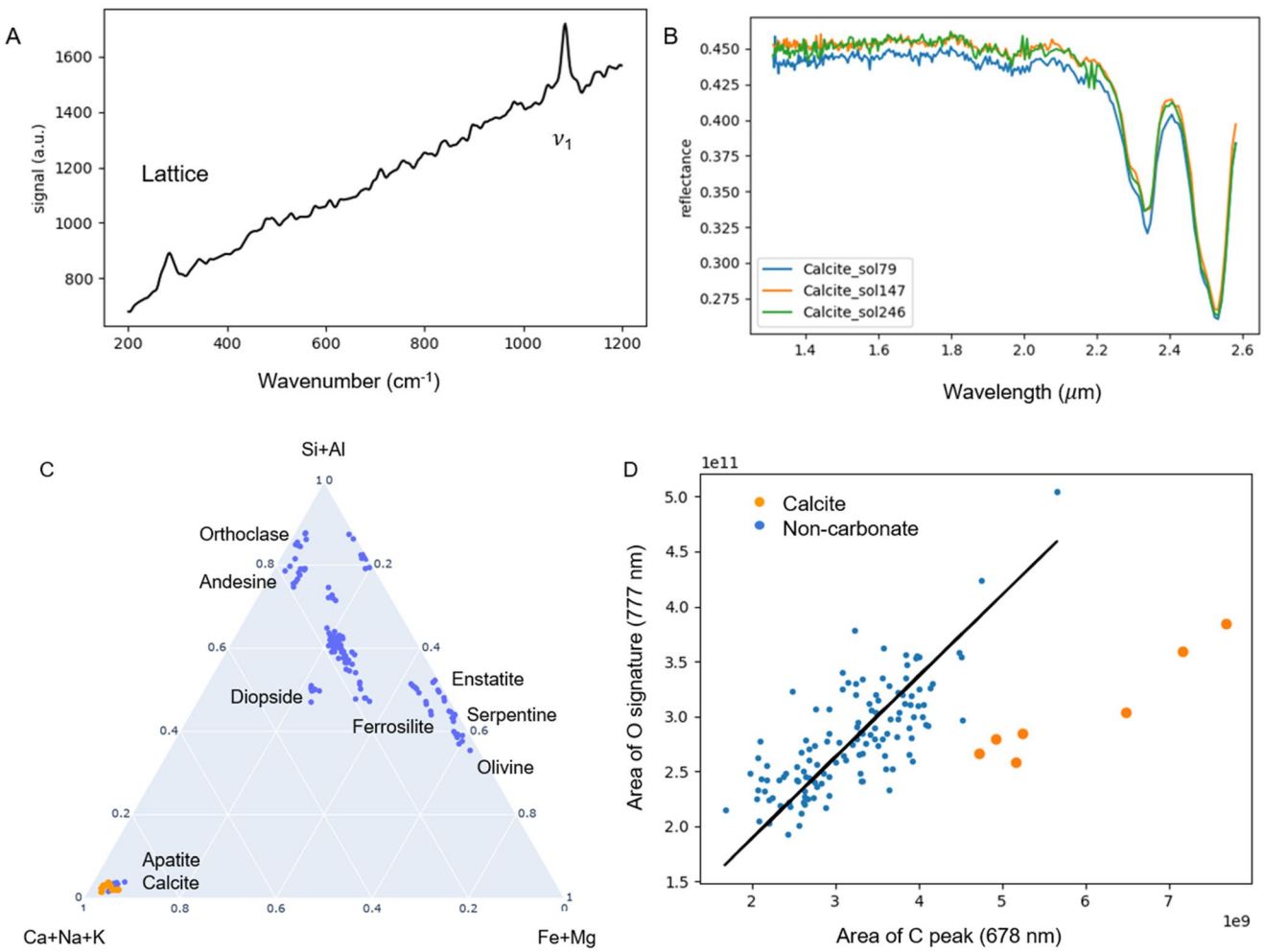

Figure 1. Carbonate detection from multi-technique analyses of the calcite SuperCam calibration target (SCCT). (a) Time-resolved Raman spectrum of the calcite SCCT obtained with an accumulation of 200 laser shots, (b) IR spectra of the calcite SCCT recorded at different times during the mission, showing characteristic 2.3 and 2.5-μm absorption bands of carbonate; (c) Si + Al/Fe + Mg/Ca + Na + K ternary plot with the major-element oxides composition data derived from Martian observations of the SCCTs; the observations of the calcite SCCT are in orange, non-carbonate SCCTs are in blue. (d) Intensities of the C and O emission lines extracted from the laser-induced breakdown spectroscopy spectra of the SuperCam calibration targets, obtained on Mars between sol 27 and sol 334. The observations of the calcite target are plotted in orange; they plot to the right of the main cloud of scattered points in blue, relative to the other SCCTs.

and the center at 2.30 μm. For the 2.5-μm band, we place the shoulders at 2.49 and 2.59 μm, and the center at 2.53 μm. For each shoulder, we use the median of the three spectral channels around the chosen wavelength; for the band center, we also use three channels for the 2.3-μm band, and two spectral channels only for the 2.5-μm band, because it is not broad enough to use three. Examples of spectral parameter fits are shown in Figure 3 and Figure S7 in Supporting Information S1.

Even though IRS enables the analysis of long-distance targets up to several km away, we focus on workspace targets in this study, that is targets observed along the rover traverse, in a radius of ∼10 m around the rover, often in conjunction with LIBS and sometimes Raman spectra.

3. Results

3.1. Application of the Multi-Technique Carbonate Detection Method to the Calcite SCCT

Up to sol 420, the calcite SCCT was analyzed seven times with LIBS, thrice with IRS, and once with TRR.

The TRR spectrum of the calcite SCCT (Figure 1a) shows the expected carbonate features: a peak at 1,085 cm^{-1} corresponding to the symmetric stretching of C-O bonds in the carbonate group (ν_1 peak, with an SNR of 220),

and a lattice vibration mode at 280 cm^{-1} (SNR ~120). The Raman signal is relatively weak, and continuum signal significant, possibly due to the small grains of the SCCT, and the relatively low number of laser shots (200). The IRS spectra of the calcite SCCT exhibits diagnostic 2.34- and 2.53-μm bands (Figures 1a and 1b). This confirms that SuperCam can observe carbonate-related absorption bands and Raman peaks on Mars. LIBS analyses of the calcite SCCT performed on seven different sols between sols 53 and 334 show very repeatable results (spectra shown in Figure S6 in Supporting Information S1) and yield MOC data consistent with the reference composition of the target measured on Earth (Table S2 in Supporting Information S1). In particular, we observe a consistently low MOC total close to 57 wt.%, as expected. Given that the SiO_2 content of the calcite SCCT is very low, this target plots in the lower part of the Si + Al/Fe + Mg/Ca + Na + K ternary diagram, close to the Ca + Na + K apex (Figure 1c). Additionally, in a plot of the 777 nm O versus the 678 nm C signatures, the C signal in the calcite SCCT is 40% higher than in non-carbonate SCCTs for a similar O-line intensity, as expected for a carbonate-rich target (Figure 1d). We observe that the C and O intensities of the calcite SCCT follow a different trend than the carbon-free SCCTs (Figure 1d), with variations of laser-target coupling between observations; these variations may be related to some small changes in the acquisition conditions, like the focus on the target or the atmospheric density. Since all SCCTs are located at similar distances from SuperCam, we directly use the median of the distance of the C/O ratio to the reference trend, obtained for the C 678 (Figure 1d) and C 723 nm (not shown here) signatures, for each SCCT observation. The resulting C score values for the calcite SCCT range between 1.87 and 5.56 for the different observations (Table S2 in Supporting Information S1), always gearter than the threshold defined in Section 2.3.1.3 for carbonate identification.

3.2. Carbonate Phases Detected in Martian Targets

To identify potential carbonates based on LIBS MOC quantification models, we plot all the LIBS analyses conducted before sol 420 by SuperCam (1,900+ points, analyzed on 225 targets) in a Si + Al/Fe + Mg/Ca + Na + K ternary diagram (Figure 2). Each point corresponds to the MOC computed on the averaged spectrum per point on the target. Most points plot between the olivine, Ca-pyroxene, and feldspar compositions. In particular, most of the points analyzed by LIBS have a SiO_2 content higher than ~40 wt.% (distribution of SiO_2 content obtained from LIBS analyses illustrated in Figure S6 in Supporting Information S1). This is consistent with our working hypothesis, that most of the analyzed targets are silicate-rich, and carbonate-poor. Moreover, the distribution of the C score values obtained on all SuperCam LIBS analyses of Martian targets, shown in Figure 2, is close to a normal distribution centered at zero and confirms the absence of non-atmospheric carbon in most of the analyzed points.

As a consequence, we can confidently use the criteria defined in Section 2.3.1, namely C score >1.28 and SiO_2 < 30 wt.%. We find 26 points that contain a significant amount of carbonates (listed in sections S1, C, M1 and M2 of Table 2).

Additionally, we investigate the depth of the 2.3-μm band versus the depth of the 2.5-μm band (BD2300 and BD2530 in Figure 3) for all IRS analyses performed by SuperCam in the rover's workspace until sol 420 (1,950+ points analyzed on 226 targets) as well as the calcite SCCT. In Figure 3 we concentrated on comparisons of spectra with the strongest band depths (i.e., 2.3-μm deeper than 2% and 2.5-μm band deeper than 1%). Candidate detections also were evaluated using the SNR of these points (generally higher than 4 for the 2.5-μm band for carbonates, as described in Royer et al., 2022) and a visual inspection of the spectra. In Figure 3b, the upper three spectra (1–3) are from points with confirmed carbonates detections; the two lower spectra (4–5) correspond to phyllosilicates without confirmed carbonate (4), and an example of spectrum where the BD2500 criterion overestimated the depth of the signatures due to noise in the spectrum (5). Confirmed carbonate detections are plotted in green in Figure 3a; other SuperCam observations are in gray; the points corresponding to the spectra illustrated in Figure 3b are circled in black in Figure 3a.

Only the confirmed carbonates demonstrate a correlation between the depths of the two bands (Figure 3a). The corresponding trend falls between the carbonate phases (SCCT and laboratory calcite and laboratory magnesite/siderite) and phyllosilicate phases (laboratory serpentinge and nontronite). We note that the observed 2.3-μm bands are deeper than the 2.5-μm bands, which is not expected for pure carbonates. This is consistent with mixtures of carbonates with phyllosilicate phases, which also have a characteristic 2.3-μm absorption (see J. L. Bishop et al., 2013; Royer et al., 2022).

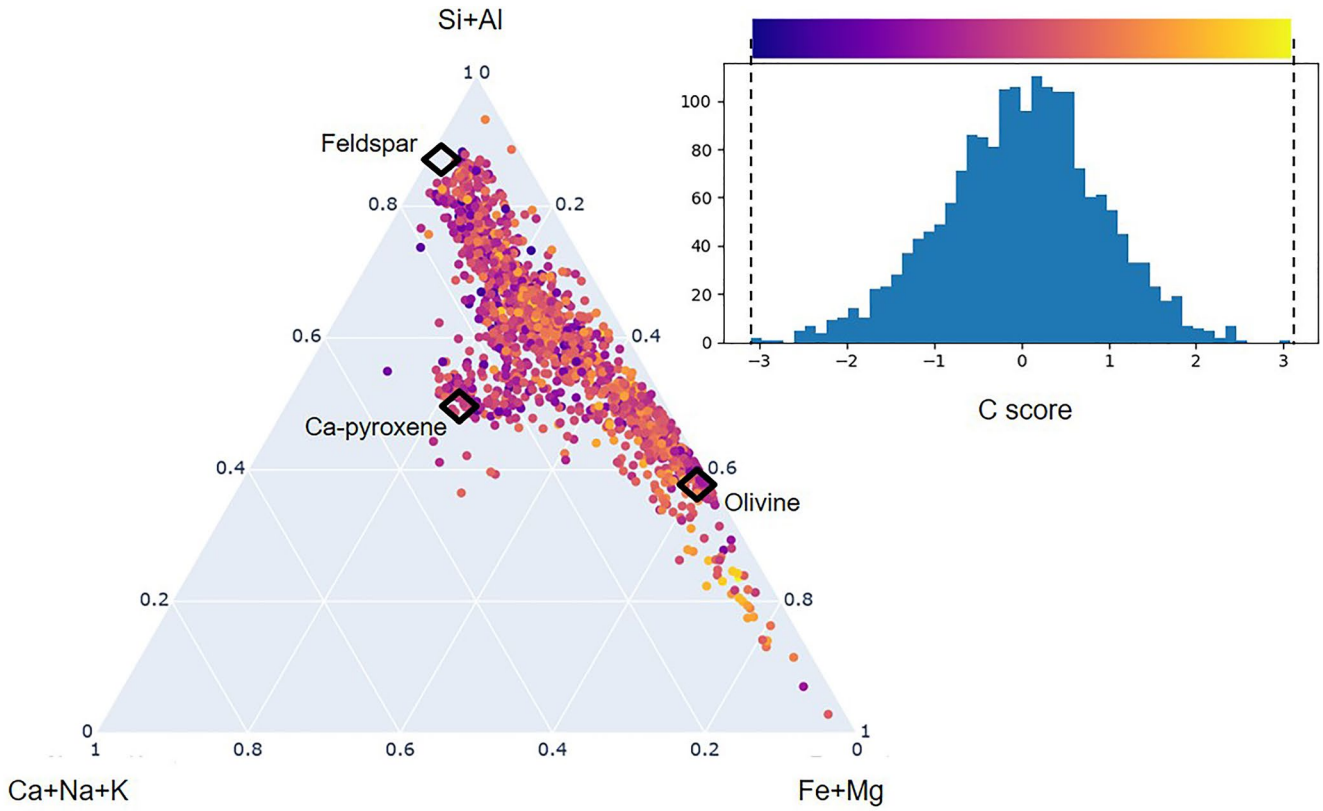

Figure 2. Overview of SuperCam laser-induced breakdown spectroscopy (LIBS) observations. On the left, distribution of all Martian targets analyzed with SuperCam LIBS up to sol 420 in the Si + Al/Ca + Na + K/Fe + Mg ternary diagram (molar contents based on major-element oxides composition). Olivine, Ca-pyroxene, and Feldspar are indicated with black diamonds. The color code is based on the C score (top right). The distribution of the C scores of all Martian targets analyzed up to sol 420 is shown on the right.

Regarding TRR, a single point was identified with a carbonate signature, out of the ~150 points analyzed on ~15 targets with this technique (discussed in Section 3.2.1.1, spectrum shown in Figure 4).

Points identified as potential carbonates using these different techniques and criteria are presented in the following sections and in Tables 1 and 2. We characterize the carbonate phases detected in the Séítah formation, in the Content member, and finally in the Máaz formation. In each unit, several rocks were abraded along the traverse of the rover, enabling more detailed observations of rock textures, without interferences from dust, erosion or coatings (Farley et al., 2020, 2022). In this study, we first look into the abraded patches, as (a) more time is generally allocated to the analysis of these targets resulting in more significant statistics, (b) these targets do not have dust or coating interfering and (c) the patches are used as proxies for the cores sampled for return to Earth in the future, and are hence of great scientific significance. We then focus on the natural surfaces analyzed remotely with SuperCam along the traverse of the rover, providing context and enabling us to identify high-potential rocks at a few meter distance from the rover, and broaden the observations derived from the abraded patches.

The compositions, distance, Mg# and C scores of all points with carbonate detections in LIBS are summarized in Table S5 in Supporting Information S1 (groups S, C, and M for points detected in Seitah, Content and Máaz, respectively).

3.2.1. Séítah

3.2.1.1. Abraded Patches

Three abrasions were performed in the Séítah formation: Garde (analyzed over sols 206–210), Dourbes (sols 259–278), and Quartier (sols 290–321). The multi-technique detection of carbonates in these three abraded patches are summarized in Table S3 in Supporting Information S1.

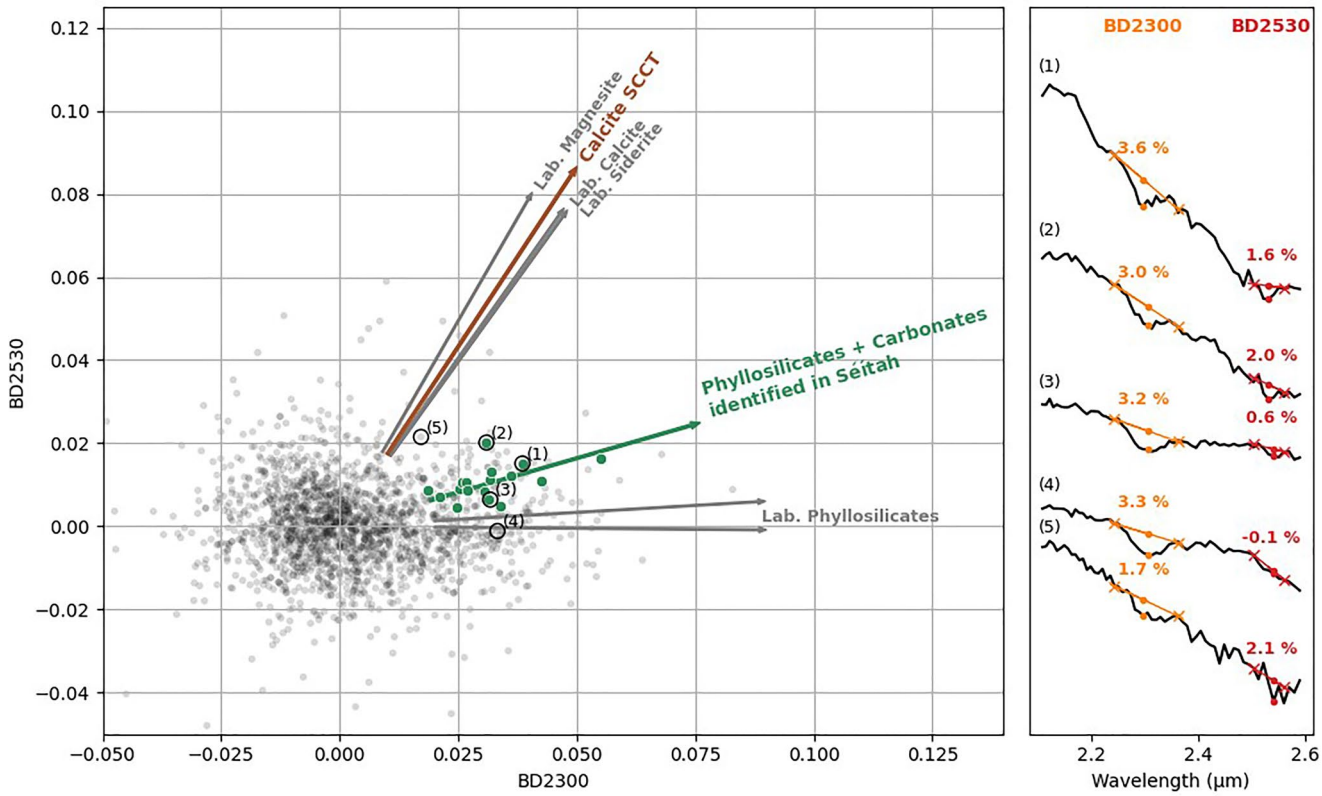

Figure 3. (a) Depth of the 2.3 and 2.5-μm bands for all infrared reflectance spectroscopy (IRS) observations up to sol 420. All SuperCam IRS observations on Martian targets are shown as small gray points; the points with confirmed IRS carbonate signatures are in green; they all belong to the Seitah fm. The trend toward Martian observations of the calcite SuperCam calibration target (SCCT) is shown in brown; for comparison, trends to reference carbonate (calcite and magnesite/siderite) and phyllosilicate (serpentine and nontronite) laboratory observations are indicated in gray. (b) Example of 2.3 and 2.5 signatures observed in i) confirmed carbonates (1: Broken_Mountain #1; 2: Mousiers_Sainte_Marie #2; 3: Garde_207 #5); (ii) a phyllosilicate (4: Garde_210 #1) and (iii) a noisy spectrum (5: Pal #2). In the two lowest spectra, we did not confirm carbonate identification.

The Garde abraded patch is the only target analyzed with SuperCam over the first 420 sols showing carbonate signatures consistently across the LIBS, IRS and TRR data (out of 16 targets analyzed with all three techniques). Four multi-technique SuperCam rasters were performed on this patch (LIBS analyses on 22 points, IRS on 27 points, and TRR on 27 points); the points where carbonates were detected are located in the RMI mosaic in Figure 4a.

Carbonate is detected with TRR in one point (Garde_209a #9, spectrum in Figure 4b). A peak at 1,087.5 ± 1.0 cm^{-1} (SNR of ~70) is interpreted as the symmetric stretching of C-O bonds in the carbonate group (ν_1 peak). No other vibrational mode characteristic of carbonate is observed. This spectrum alone is not sufficient to tightly constrain the composition of the detected carbonate phase, due to the low SNR (only slightly above our threshold value of 50), and detection of a single mode, but the Raman shift of the ν_1 peak is generally consistent with a siderite-magnesite solid solution (Rividi et al., 2010). Additionally, in the same Raman spectrum, the broad band centered around 400 cm^{-1} is attributed to the Raman signal of the amorphous silica of the optical fiber of the SuperCam instrument. A peak at ~830 cm^{-1} is interpreted as the spectrally unresolved doublet of olivine (unresolved due to low signal), corresponding to stretching in the SiO_4 tetrahedra. While olivine has been detected by Raman in other points on the abraded patch and other targets in Séítah, (Beyssac et al., 2023) Garde_209a #9 is the only detection of carbonate with the SuperCam Raman instrument so far.

Carbonate is also detected with IRS on the Garde abraded patch (in particular in points Garde_209a #8 and, to a lesser extent, Garde_207 #5 and 8, and Garde_210 #7, spectra shown in Figure 4c), together with olivine and phyllosilicates. This is indicated by: (a) a broad absorption band at 1 μm, observed in SuperCam's spectral ranges below 0.85 and above 1.3 μm, which can be attributed to olivine, siderite, or a combination of both; (b) a broad 2.3-μm absorption band, attributed to a combination of phyllosilicates and carbonates; and finally (c) a small

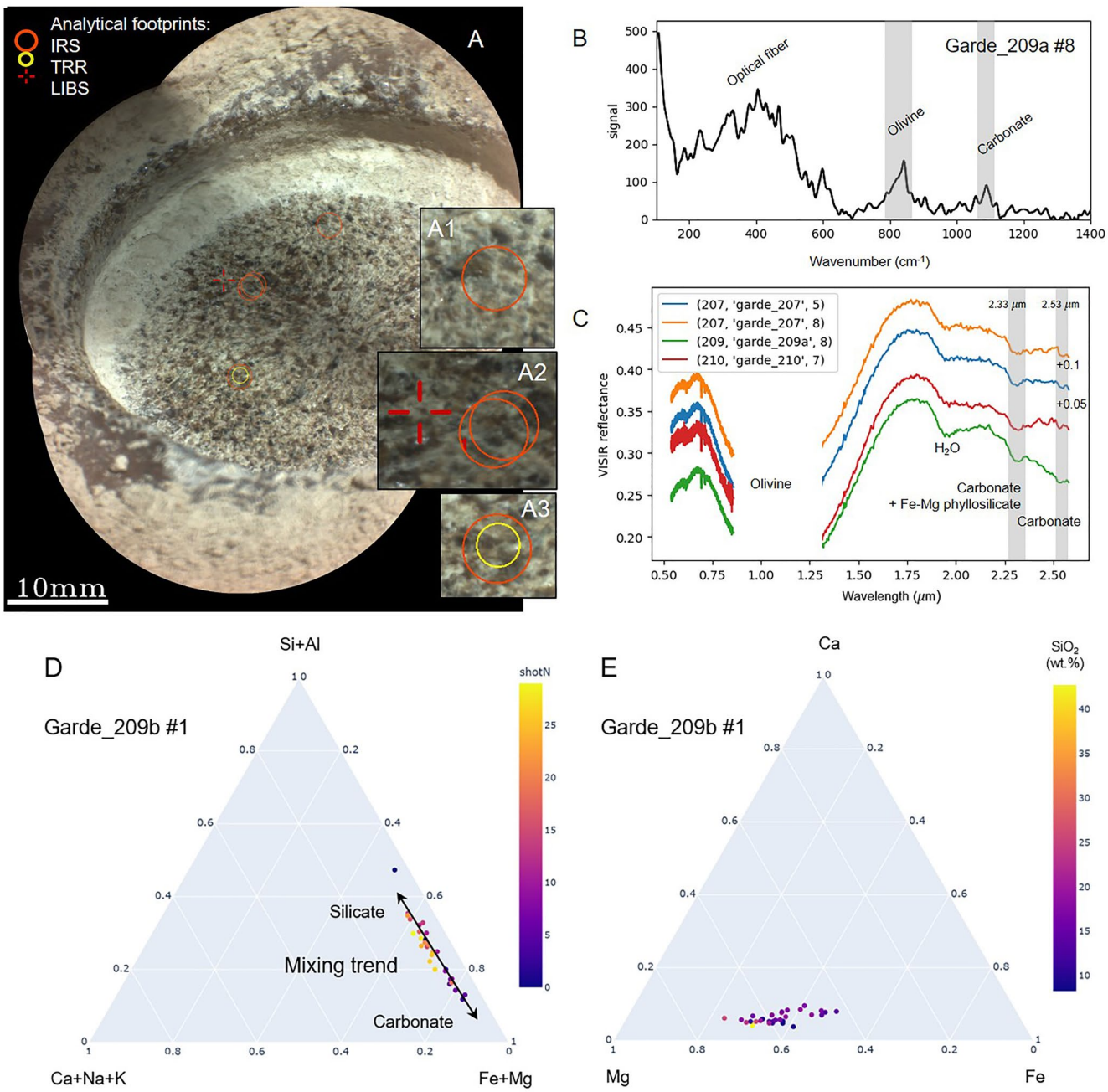

Figure 4. Detection of carbonate spectroscopic signatures in the Garde abraded patch. (a) Mosaic of remote micro-imager images acquired on the Garde abraded patch with the points and corresponding analytical footprints for points where carbonates are detected: with laser-induced breakdown spectroscopy (LIBS) (red cross): Garde_209b #1; with time-resolved Raman (TRR) (yellow circle): Garde_209a #9; with infrared reflectance spectroscopy (orange circles): Garde_207 #5 and 8, Garde_209a #8 and Garde_210 #7. (A1-3) Close-ups on the carbonates detected in Garde_210 #7 (A1), Garde_207 #5 and 8 and Garde_209b #1 (A2), and Garde_209a #8 (A3). (b) TRR spectrum of Garde_209a #9, with a contribution from the optical fiber (200–500 cm^{-1} mostly) and signatures of olivine (unresolved doublet between 820 and 840 cm^{-1}) and carbonate (ν_1 mode observed at 1,087.5 cm^{-1}). (c) IR spectra of Garde_207 #5 and 8 (plotted with small offsets to reduce overlap, indicated to the right of the plot), Garde_209a #8 and Garde_210 #7 with signatures of olivine (broad band centered around 1-μm), hydration (1.9-μm band), and carbonate + phyllosilicate in 2.33- and 2.53-μm bands. (d–e) LIBS shot-to-shot observations on Garde_209b #1, reported in ternary plots of the molar contents. (d) Si + Al/Fe + Mg/Ca + Na + K ternary diagram. Mixing trend between a carbonate and a silicate endmember visible in the data and highlighted with the black arrow. The color is based on the shot number. (e) Ca/Mg/Fe ternary diagram, the color is based on the SiO_2 content (in wt.%).

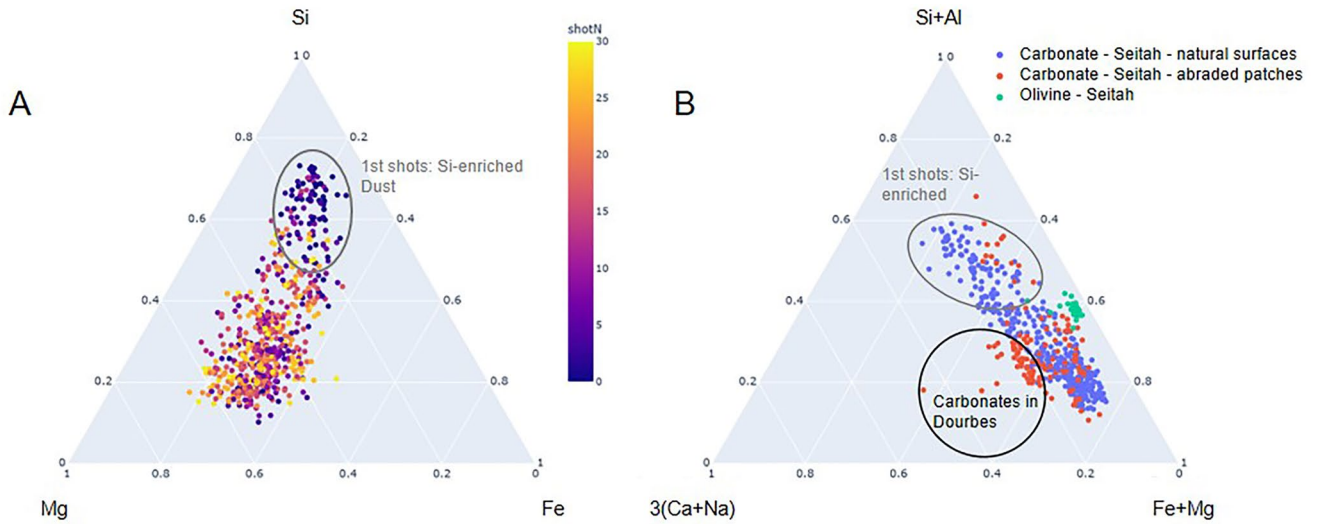

Figure 5. Shot-to-shot molar composition of carbonate detections in the Séítah formation (both abraded patches and natural surfaces, up to sol 420). (a) Si/Mg/Fe ternary diagram, color-coded to the shot number. First shots are circled in gray to show dust contribution. (b) Si + Al/3(Ca + Na)/(Fe + Mg) ternary diagram, color coded to the nature of the target: blue and red respectively for carbonate-bearing natural surfaces and abraded patches in Séítah and green for an olivine grain (Pra_Loup #9, analyzed on sol 323).

2.5-μm band, which enables us to discriminate carbonates from phyllosilicates (Mandon et al., 2022). Closer views of the 2.3 and 2.5-μm absorption bands and fitted parameters are presented in Figure S7 in Supporting Information S1. In addition, a 1.9-μm band, characteristic of H_2O is detected in the IR spectra.

Finally, carbonate was detected with LIBS (in Garde_209b #1, Figures 4d and 4e) evidence to support this conclusion includes (a) the intensity of the C line is high and the C to O ratio is consistent with non-atmospheric carbon (C score of 1.64); (b) the Si abundance (15.3 wt% SiO_2) is too low for any pure silicate mineral; (c) the total of the MOC of 79 wt% is consistent with elements (possibly C and O from CO_3) not taken into account in the quantification; (d) high iron and magnesium contents (26.7 wt.% FeOt and 28.6 wt.% MgO) for this point suggest a phase such as Fe-Mg carbonate. In particular, the shot-to-shot trend in the ternary diagram is consistent with a mixture of a Fe-Mg carbonate with a silicate phase (Figure 4d). The Mg# of the shots varies between 0.54 and 0.73. The shots with the lowest Si + Al% (<0.2, i.e., corresponding to the highest carbonate content) have an Mg# around 0.60 and 3–4 wt.% CaO. Interestingly, the amount of CaO is relatively stable throughout the 30 shots, indicating that the calcium is present in both carbonate and silicate endmembers (Figure 4e).

For the other two abraded patches analyzed in the Séítah fm, we summarize the detections here. RMI mosaics of these two abraded patches, indicating the location of the detected carbonates are presented in Figures S8 and S9 in Supporting Information S1. The shot-to-shot composition of the carbonates detected with LIBS and IRS spectra are illustrated in Figure S10 in Supporting Information S1. Dourbes is the second patch abraded in the Séítah formation. Four multi-technique SuperCam rasters were performed on this patch (LIBS analyses on 28 points, IRS on 24 points, and TRR on 16 points). Carbonate signatures were detected with both LIBS (Table 2-S1) and IRS (Table 1). Only olivine was conclusively detected with TRR. Finally, 38 points were analyzed with LIBS and IRS, and 34 points with TRR on the Quartier abraded patch (sols 294–321). Signatures consistent with carbonates were only detected in a single point with LIBS, two points with IRS and none with TRR.

3.2.1.2. Natural Surfaces

Thirteen points analyzed with LIBS on natural surfaces in the Séítah formation (out of 768) have both a high C score (>1.28) and low SiO_2 content (<30 wt.%). These points, listed in Table 2-S1, have low Al_2O_3 (<7 wt.%, and <5 wt.% in 11 out of these 13), low calcium content (CaO ∼1–5 wt.%), with Mg# between 0.42 and 0.70 (based on averaged spectra).

Taking a closer look at these points, using the shot-to-shot MOC data (Figure 5), we observe that many of the first shots (blue-purple markers in Figure 5a; gray ellipse in Figures 5a and 5b) are Si-enriched, with generally lower

Mg#. This is consistent with the signature of dust, as shown elsewhere (Lasue et al., 2022). We do not consider these shots further, but focus on the rest, which likely sampled carbonates.

We observe some spread of Ca and Na contents among the plotted shots (Figure 5b), but most interestingly, carbonate-rich points are relatively enriched in Ca and Na compared to an olivine grain (green markers, Pra_Loup #9 analyzed on sol 323, RMI in Figures 6c and 6e), which we use as a local reference for olivine MOC composition. We also observe that the shots acquired on abraded patches and natural surfaces (red and blue points in Figure 5b, respectively) generally overlap, although the carbonate-rich points detected in the Dourbes abraded patch have higher Ca content than most other points. Note that the Ca content is still low overall (Text S3 and Figure S11a in Supporting Information S1). Additionally, we note that the H signal in the carbonate-bearing points is higher than the average H signal observed in all LIBS observations (Figure S11b in Supporting Information S1).

Regarding the carbonate detected in non-abraded targets, the RMI images contextualizing spectroscopic analyses show granular textures, with isotropic distributions of mostly fine (<1 mm) to medium (<5 mm) grain-sizes, as observed in most Séítah rocks (Beyssac et al., 2023; Wiens et al., 2022). However, we could not precisely locate the distribution of carbonate-bearing points with respect to those grains.

In addition to these 13 points, other points analyzed with LIBS are consistent with carbonates, or at least with mineral mixtures including carbonates, when observing the shot-to-shot data. The averaged spectra on these points do not match our criteria, and single-shot data are noisier and harder to interpret. Therefore, identifying these points requires a more detailed analysis. Below are two examples of such points: Brac_246 #5 and Pra_Loup #5 (RMI images of these targets are shown in Figures 6c–6f; list of corresponding detections in Table 2-S2).

Point Brac_246 #5 (sol 246, RMIs in Figures 6d and 6f) has a C score of 1.17, and therefore does not meet on average the criteria we set for carbonate identification; additionally, its Al_2O_3 content is slightly higher than expected for pure carbonates (~7 wt.%). However, the shot-to-shot data show that the LIBS analyses probed two different mineral phases (Figure 6a). More precisely, the first ~15 shots are consistent with indurated dust, which has been detected in multiple targets in Jezero Crater (Garczynski et al., 2022). Then the following 15 shots are relatively poor in Si, and Al, (as well as Ca, H, and Ti), and enriched in Fe, and Mg, (as well as C), which is consistent with carbonates. Considering that the C score is only slightly below the threshold, it could be consistent with the C contribution of a carbonate phase in only 15 shots out of 30.

Pra_Loup is a target analyzed on sol 323 in which we identified carbonate in point #6 (Table 2-S1, RMIs in Figures 6c and 6e). By contrast, in point #5 of the same target, the SiO_2 content of 40.4 wt.% is significantly higher than our threshold value. The two points #5 and #6 reported in Figure 6b appear to be mixtures, with different proportions of the same two mineral phases, that is, a phase belonging to a siderite-magnesite solid solution, on the low-Si end, and an unidentified silicate on the other end. In both points, the Si-rich shots are the deepest, indicating that the carbonate phase is located toward the surface of the target. The C scores in points #5 and 6 are 1.51 and 3.72, respectively, which is also consistent with the presence of carbonate, with a higher average carbonate content in #6.

In these two examples, using the shot-to-shot data enables the identification of carbonates in mixtures, either at surface, as in Pra_Loup #6 (Figure 6b), or below what could be another coating, as in Brac_246 #5 (Figure 6a), even when the average data is not clearly indicative of carbonate, based on our criteria. Moreover, these analyses help characterize the composition of the carbonate phases mixed with another mineral phase by separating the major-oxides associated to the carbonates versus those contained in the phases in mixture.

With IRS, we identify carbonate signatures in eight points analyzed on natural surfaces (plotted in green in Figure 3a, listed in Table 1). Similarly to the IRS spectra of carbonates identified in abraded patches, the spectra of these nine points show 2.3-μm band broader and deeper than the 2.5-μm bands, which we attribute to associated carbonates and phyllosilicates (spectra in Figure S12 in Supporting Information S1). The 2.5-μm bands are all slightly above noise level. The spectra also show broad absorption bands around 1 μm consistent with olivine, and 1.9-μm bands characteristic of H_2O.

There is no overlap of targets with carbonate detection with LIBS and IRS on natural surfaces, but some targets belong to the same outcrops. Interestingly, three of the eight points where carbonate signatures were detected by IRS correspond to a single target, in one of the few rocks analyzed in the portion of Seitah located at the toe of

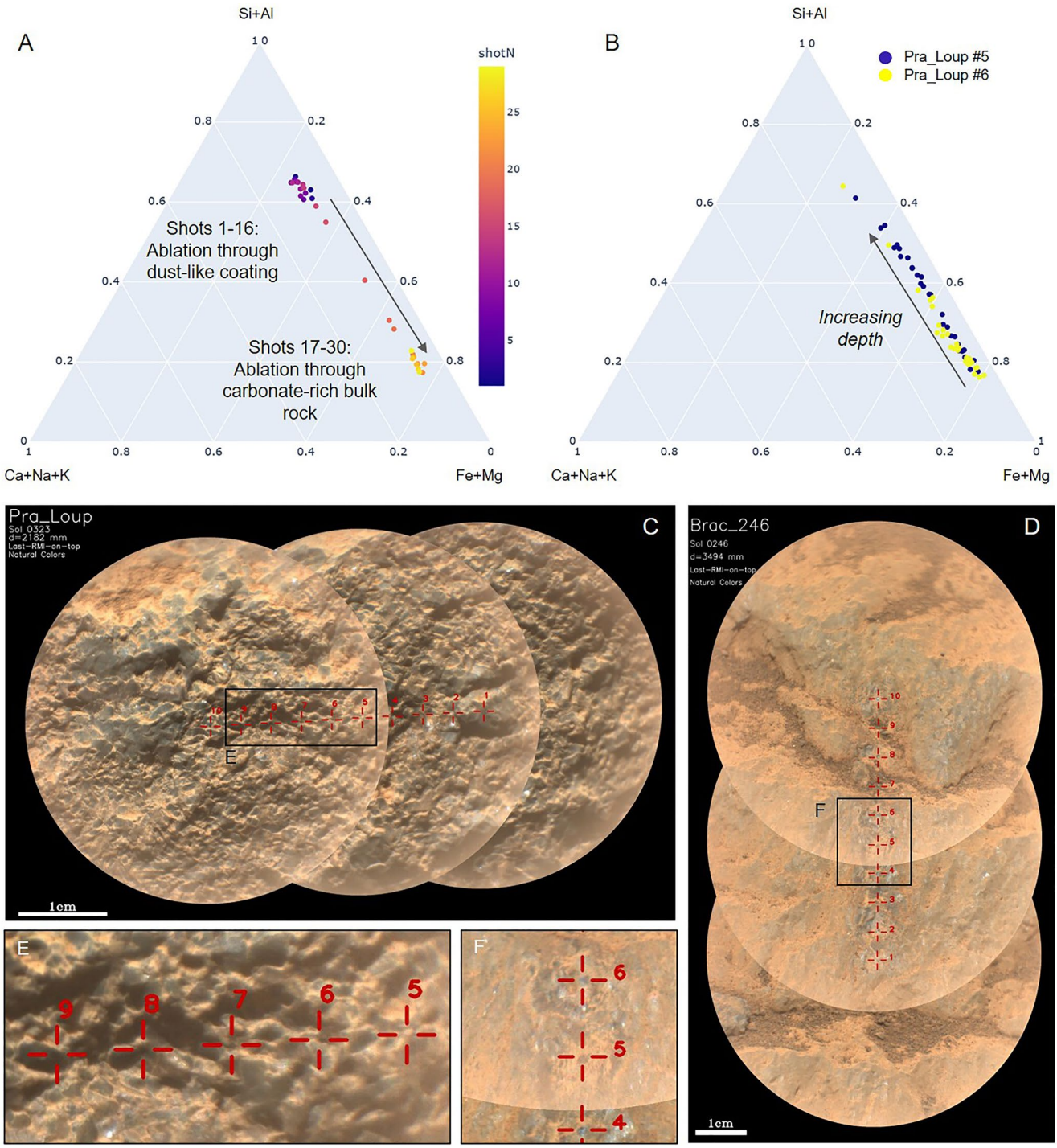

Figure 6. (a–b) Compositional depth trends (molar composition); the arrows indicate increasing depth (a) Brac_246 #5 shot-to-shot composition data, showing two different mineral phases probed in the first ~15 and last ~15 shots; (b) Pra_Loup #5 and #6, showing similar mixing trends; the Si content increases with depth. (c–f) RMI images of the Pra_Loup and Brac_246 targets; close-ups of points of interest in E and F; point #9 of Pra_Loup sampled an olivine grain.

the current delta (Broken_Mountain, analyzed on sol 420; spectra in Figure S12 in Supporting Information S1, RMI mosaic in Figure S13 in Supporting Information S1). LIBS data in this target show a couple points with low SiO_2 content (around 15 wt.% in #6 and 7), but their C score (around 0.45) does not indicate carbonate; this discrepancy may be due to the different analytical footprints of LIBS and IRS.

Table 1
List of Carbonate Detections Based on Infrared Reflectance Spectroscopy Data

Sol	Target name	Point	Unit	Description
173	Entrevaux	5	Séítah	Dark rock surface
178	Aiguines	10	Séítah	Dusty rock surface
205	Mairola	4	Séítah	Dark rock surface
207	Garde_207_scam	5	Séítah	Abraded patch
207	Garde_207_scam	8	Séítah	Abraded patch
209	Garde_209a_scam	8	Séítah	Abraded patch
210	Garde_210_scam	7	Séítah	Abraded patch
213	Moustiers_Sainte_Marie	2	Séítah	Dark rock surface
242	Gion	9	Séítah	Dark rock surface
268	Dourbes_268	1	Séítah	Abraded patch
295	Quartier_295_scam	1	Séítah	Abraded patch
297	Quartier_297_scam	6	Séítah	Abraded patch
319	Robine_tailings_319	3	Séítah	Abrasion tailings
420	Broken_Mountain	2	Séítah	Dark rock surface
420	Broken_Mountain	3	Séítah	Dark rock surface
420	Broken_Mountain	6	Séítah	Dark rock surface

Note. The corresponding spectra are shown in Figure 4 and Figures S10 and S12 in Supporting Information S1; the points listed here are plotted in red in Figures 8b and 8c.

3.2.2. Content Member

In the Content member, two points (out of 46) have high C scores and low SiO_2 content (Table 2-C). These points also have a high Ti content, one of them being among the points with the strongest Ti signal among the LIBS analyses performed up to sol 420 (possibly as high as ∼30 wt.% TiO_2 in some points). Therefore, these points could be mixtures of Ti-Fe oxides, such as ilmenite, with siderite (Mg# of 0.09–0.16).

No evidence for carbonate was found in the IRS data of the Content member.

3.2.3. Máaz

Four rocks were abraded in the Máaz formation: Guillaumes (sols 160s), Bellegarde (sols 180–190), Montpezat (sols 345–350) and Alfalfa (sols 370s). Among the 68 LIBS points, 63 IRS points and 62 TRR points analyzed on the clean abraded patches, none matches our criteria for carbonate identification.

Moreover, no carbonate was detected with IRS in natural surfaces in Máaz. By contrast, using LIBS, eight points (out of 687) analyzed on natural surfaces in the Máaz formation match the pre-defined criteria for carbonate detection (C score > 1.28 and SiO_2 < 30 wt.%). Additionally, they have low MOC totals (66–80 wt.%). We distinguish two different categories among these eight points, presented below: the first category is consistent with siderite in mixture with Fe/Ti oxides (Table 2-M1); the second category is enriched in Mg (Table 2-M2).

First, five out these eight points (listed in Table 2-M1) have low Mg# (0.10–0.14), in line with the overall low Mg content in the Máaz fm. Their CaO content is 3.4–6.3 wt.%. Combined with C scores of 1.6–2.0, this is consistent with siderite. These points also have elevated Ti contents (Table S5 Supporting Information S1). These points are very similar to those found in the Content member, and seem consistent with a mixture of Fe-Ti oxides (in varying amounts) with siderite.

In the targets where these siderites were detected, other points are consistent with Fe/Ti oxides (ferrihydrite or ilmenite). To distinguish these phases, we rely on the C and H signals, as well as the interpretation of the sum of major oxide content. Iron oxy-hydroxides are identified based on low SiO_2 content (a few percent), high FeOt (∼80 wt.%), a very strong H signal and low C scores (and confirmed with VISIR data, see Mandon et al., 2022). By comparison, siderite-bearing points are characterized by a lower FeO content (25–50 wt.%), a low MOC total and a high C score: moreover, a low H signal indicates that the low MOC total cannot be attributed to hydration.

The second category of carbonate detections in Máaz consists in three points, listed in Table 2-M2. We discuss one of these in details here, and the same analytical strategy can be applied to the other two, yielding comparable results.

In the Alk_es_disi target (sol 91, Figure 7), points #3–5 of the raster have a low SiO_2 content (∼22 wt.%), an elevated MgO content (∼28 wt.%, which is very rare for rocks in the Máaz formation) and a relatively low MOC total (∼76–78 wt.%). Moreover, they have a high H signal, a strong CaF signature and elevated S signal, indicating probable Mg-sulfates, possibly mixed with iron oxides and fluorite (Meslin et al., 2022). Interestingly, point #8 in this target shares a large part of these characteristics; in particular, its MOC is very similar to points #3–5, including the unusually high MgO content (Figure 7e). However, point #8 is not on the same brownish patch as points 3–5 (Figure 7b), but the RMI shows that instead it sampled a thinner brownish coating on the rock (Figure 7c). It shows a much higher C score (1.74 in #8 vs. −0.63 to 0.85 in #3–5), a chlorine peak but no visible S signature. This rock thus appears to be coated with a mixture of salts, including sulfate and carbonate: the thick patch sampled with point #3–5 is consistent with a mixture of Mg-sulfates with iron oxides (Meslin et al., 2022) but the thinner coating analyzed with point #8 matches a Fe-Mg-carbonate, with high Mg# (0.83; actually the highest Mg# in all the carbonate-containing points presented in this study).

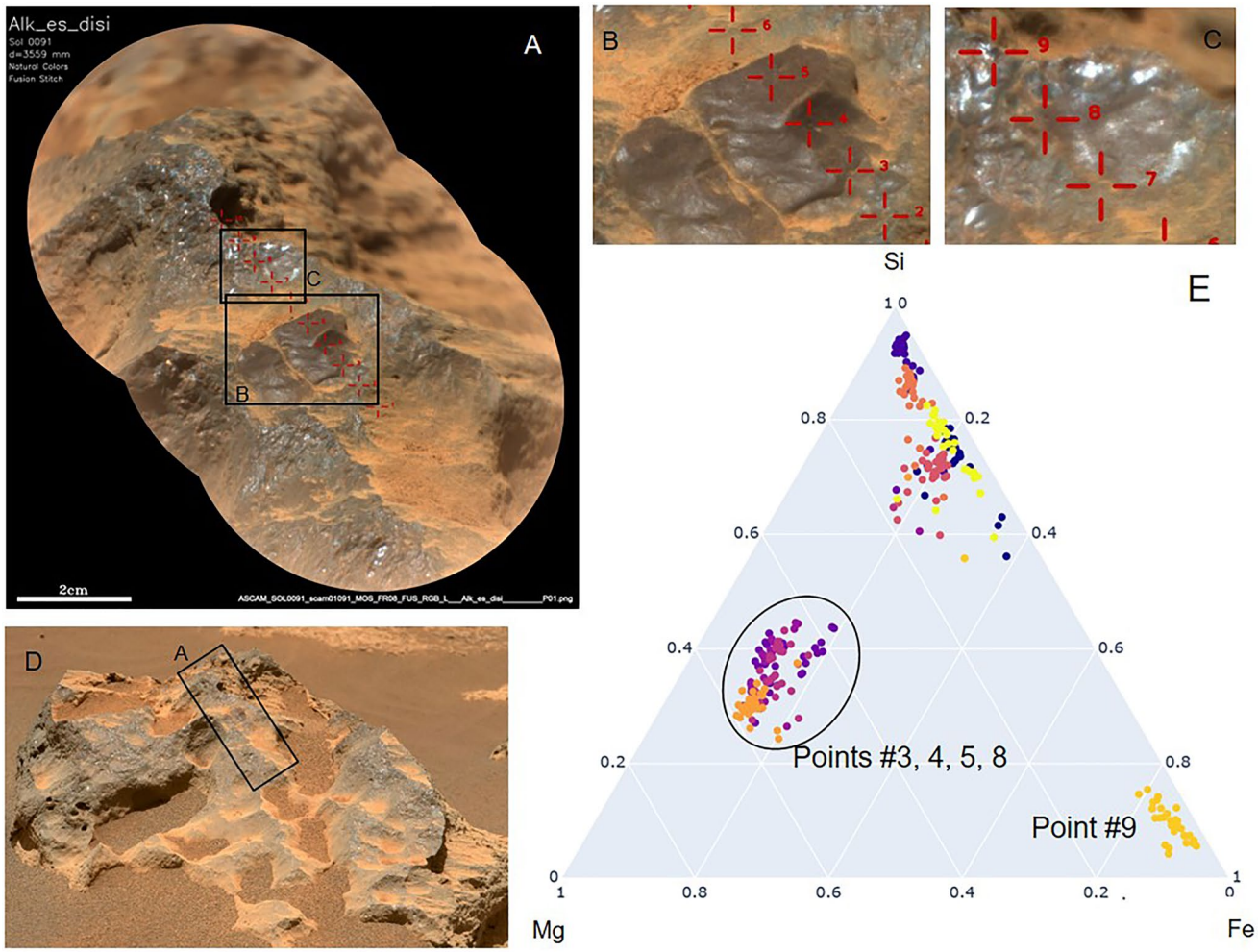

Figure 7. Alk_es_disi target (sol 91, Máaz formation). (a) remote micro-imager mosaic with laser-induced breakdown spectroscopy footprints (red) and locations of the close views displayed in (b and c). (b–c) zoom on areas of interest. (d) Context image of the rock recorded by ZCAM. (e) Shot-to-shot molar elemental abundances (derived from MOC) of Alk_es_disi, highlighting the different compositions of the salt-bearing points (#3–5 and 8 in Alk_es_disi) compared to the rest of the points analyzed on this target, especially regarding MgO; point #9 sampled a Fe-oxy\hydroxyde.

Similarly, the Neeznaa and Pont targets also show (a) sulfates and carbonates in the LIBS data, and (b) an enrichment in MgO in the sulfates as well as in the carbonates. Shot-to-shot compositions are shown, and compared to Alk_es_disi in Figure S14 in Supporting Information S1; the RMI mosaics acquired on the Pont and Neeznaa targets are shown in Figure S15 in Supporting Information S1.

Additionally, as in Séítah, we can identify a few points with average compositions that do not quite fit our thresholds, but whose shot-to-shot data probably indicate carbonates in mixtures; some examples are listed in Table 2-M3; one of them is illustrated in Figure S16 in Supporting Information S1.

3.3. Summary of Carbonate Detections With SuperCam in the Maaz and Seitah Formations

SuperCam LIBS, IRS and TRR data reveal several different carbonate phases along the rover traverse, in both Máaz and Séítah formations (Figure 8).

All the carbonate detected in Séítah rocks, on both abraded and natural surfaces, are consistent with the magnesite-siderite solid-solution, with a low CaO content (1–5 wt.%) and Mg# of 0.42–0.70. The proportion of points with carbonate detection is higher in abraded patches than on natural surfaces (4.5% and 1.7% of the analyzed points, respectively; summarized in Table S4 in Supporting Information S1). Carbonate phases are associated with (a) olivine, both in the IRS and TRR spectra, and at the scale of the target or the outcrop in LIBS data; (b)

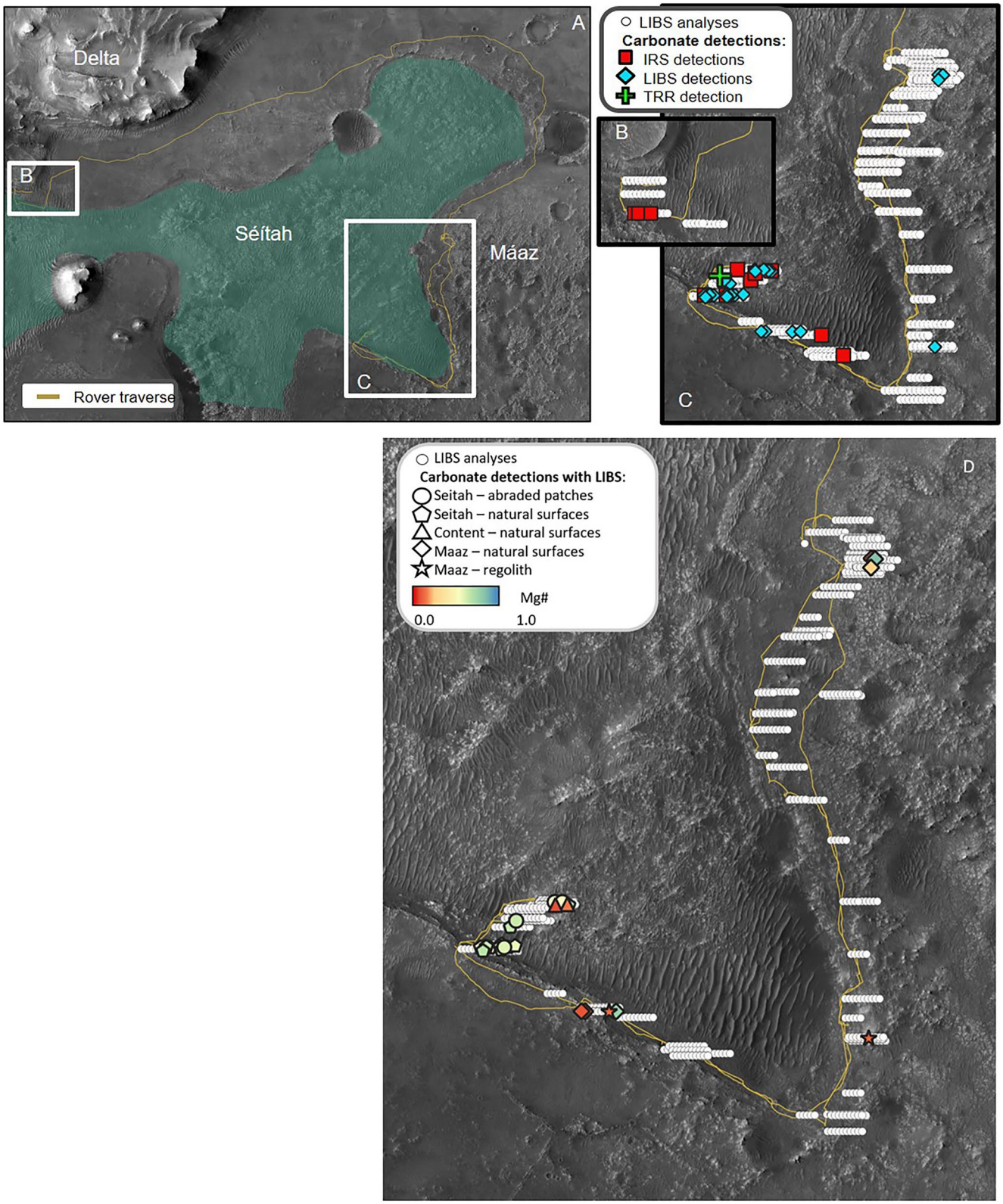
A
Delta
B
Séítah
Máaz
C
Rover traverse
LIBS analyses
Carbonate detections:
IRS detections
LIBS detections
TRR detection
B
C
LIBS analyses
Carbonate detections with LIBS:
Seitah – abraded patches
Seitah – natural surfaces
Content – natural surfaces
Maaz – natural surfaces
Maaz – regolith
Mg#
0.0
1.0
D

Figure 8.

Table 2
Carbonate Detections With Laser-Induced Breakdown Spectroscopy

	Details in section	Sol	Target name	Point	Unit	Surface
S1	3.2.1 (Abrasion in 3.2.1.1, others in 3.2.1.2)	203	Rourebel	5	Seitah	
		209	Garde_209b_scam	1	Seitah	Abrasion
		242	Nans	9	Seitah	
		268	Dourbes_268	5	Seitah	Abrasion
		268	Dourbes_268	7	Seitah	Abrasion
		286	Bezaudun	6	Seitah	
		287	Castiglione	8	Seitah	
		297	Quartier_297_scam	7	Seitah	Abrasion
		309	Jabron_309	3	Seitah	
		323	Pra_Loup	6	Seitah	
		323	Pra_Balou	2	Seitah	
		324	Amen	10	Seitah	
		327	Miassol	1	Seitah	
		333	Toudon	2	Seitah	Regolith grain
		333	Toudon	9	Seitah	Regolith grain
		335	Chabran	1	Seitah	
		338	Calandre_338	6	Seitah	
S2	3.2.1.2	202	Issole	10	Seitah	
		246	Brac_246	5	Seitah	
		323	Pra_Loup	5	Seitah	
C	3.2.2	250	Hotel	8	Content	
		280	Thouron	5	Content	
M1	3.2.3	90	Tsostid_tsaadah_90	7	Maaz	
		145	Croix	6	Maaz	Regolith grain
		185	Chambares	8	Maaz	Regolith grain
		193	Souche	1	Maaz	
		193	Pont	2	Maaz	
M2	3.2.3	91	Alk_es_disi	8	Maaz	
		92	Neeznaa_scam	7	Maaz	
		193	Pont	10	Maaz	
M3	3.2.3	89	Taa-Ihaaih	2	Maaz	
		151	Reglet	2	Maaz	

Note. The points are grouped by detection categories, as described in the Sections 3.2.1–3.2.3. Carbonates detected in Séítah, Content and Máaz are in groups S, C, and M, respectively. Points in S1, C, M1, and M2 meet the C score and SiO_2 criteria on the average data. Points in S2 and M3 have some shots consistent with carbonates, although their averages do not meet our criteria. The points listed here are represented in Figures 8b–8d; the details of the compositions, Mg# and C scores are available in Table S5 in Supporting Information S1.

Figure 8. Carbonate detections with SuperCam along the rover traverse (brown line). (a) The Seitah fm is highlighted in green. (b–c) Close-ups on the few targets analyzed in Cf-f2 after the drive campaign around Seitah (b, including Broken_Moutain) and the traverse corresponding to the Crater floor campaign (c). The white markers show all laser-induced breakdown spectroscopy (LIBS) analyses, larger, colored markers show carbonate detections (with LIBS: blue-filled diamonds, IRS: red squares and TRR: green plus).(d) LIBS detections only (small white markers). Only the carbonate detections are color coded using Mg#. Abraded and natural surfaces are indicated by distinct large symbols. The IRS and LIBS detections illustrated in (b–d) correspond to the points listed in Tables 1 and 2, respectively.

phyllosilicates, inferred from the broadness of the 2.3-µm band, and the relative depths of the 2.3- and 2.5-µm bands in IRS. This is consistent with the composition derived from mixing trends observed in shot-to-shot LIBS data: carbonates are mixed with a mineral phase relatively enriched in Ca, Na as well as Al + Si, compared to olivine.

In Séítah, carbonates are detected—in low abundance, but they seem ubiquitous—in rocks that are characteristic of the formation—interpreted as an olivine cumulate. In Máaz, however, we find them mostly in chemical outliers: (a) Ti-enriched rocks, and (b) points with unusually high Mg content and associated with sulfates and coatings. Carbonates in Máaz are only detected with LIBS, not in IRS or TRR data, and only on natural surfaces—no detection on the Guillaumes, Bellegarde, Montpezat or Alfalfa abraded patches. They are mostly consistent with siderites; in this case, they have a very low Mg#, comparable to the bulk rocks where they are found, similarly to what is seen in Séítah. Three points showing elevated Mg content and where we find carbonates in coatings appear as an exception and are spatially associated with sulfates.

None of the carbonate detection described here matches a pure carbonate; in LIBS, TRR and IRS data, the detected carbonate phases are always mixed with some silicates, and sometimes additional phases, such as Fe-Ti oxide in the Content member, and some Maaz targets, or Fe-Mg-sulfates.

Several of the carbonate-containing targets show a significant LIBS H signal, as well as deep 1.9-µm H_2O bands in IRS, suggesting some hydration. However, in most cases, it is not clear if it is the carbonate phase itself and/or the associated silicate phase that is hydrated. On Garde, the Raman spectrum suggests an anhydrous carbonate phase instead of an hydrated one such as hydromagnesite.

4. Discussion

Here we show that SuperCam has confidently detected several occurrences of carbonate mineral phases in situ in the Jezero crater. This is consistent with several detections performed by PIXL and SHERLOC on abraded patches, two other Mars 2020 instruments (Section 4.2.1). SuperCam is especially adapted to carbonate detection for two main reasons: (a) C signal is detected in LIBS and carbonates are directly detectable in TRR and IRS; the combination of these techniques improves the confidence on the detection of carbonates, especially in the case of weak signals; (b) these techniques also enable the characterization of the composition of both the detected carbonates and the mineral phases in mixtures.

Here, we first discuss the method presented in this article to identify carbonates in SuperCam multi-technique data, before further discussing the consistency of these detections and the implications of these analyses regarding involved geochemical processes.

4.1. Challenges and Successes of In Situ Detection and Characterization of Carbonates With SuperCam

We defined a couple of criteria to identify carbonate-bearing points in SuperCam LIBS data: C score >1.28 and SiO_2 < 30 wt.%. Additionally, we consider some indicators, which help reinforce the detections. In particular, low MOC totals are indicative of non-quantified oxides and high Fe + Ca + Mg is expected in most carbonates, so are overall low Al, Na, and K. In addition, a complementary assessment of minors—including C, but also S, H, Cl, P, etc.—is required to reliably identify carbonates. Otherwise, it is impossible to discriminate between carbonates, sulfates, phosphates, Cl-bearing phases or even Fe-oxyhydroxides, which also have low SiO_2, low MOC totals, elevated Ca + Fe + Mg and low Al, Na and K. In this study, we propose a C score to characterize the carbon content of Martian targets. Similarly, Meslin et al. (2022) uses a S score. In parallel, some work is ongoing within the SuperCam team to quantify or characterize more minor elements.

We discuss briefly the limits of (a) our MOC-based criterion and indicators, and (b) our C characterization.

4.1.1. Limits of MOC-Based Carbonate Detection

We highlight three main caveats regarding our MOC-based analyses:

1. *A bias toward high carbonate contents and/or mixtures of carbonates with relatively low SiO2-containing silicates*: the upper SiO_2 limit of 30 wt.% criterion may limit the efficiency of carbonate detection. In fact, mixtures of carbonates with a silicate phase having a (much) higher SiO_2 content than olivine may have an overall SiO_2 content higher than 30 wt.% and therefore be discarded by our screening approach. Overall, the

limit of detection of carbonates by this approach depends somewhat on the SiO_2 content of the phases mixed with carbonates. We note that points with high C scores (>1.28) are found with very diverse compositions, including orthopyroxenes and clinopyroxenes as well as more felsic compositions. If a high C score were by itself a sufficient indication of carbonates, then this would mean that SuperCam probed carbonate phases mixed with a wide variety of minerals. However, the threshold we set on the C score value expectedly yields about 10% false positives; to identify these, we combine this criterion with other above-mentioned criteria. Additionally, the analysis of shot-to-shot data helps identify carbonates mixed with various phases, including Si-rich ones, when the grain size is not too small and/or the mixture not homogeneous at the ablation scale. Further laboratory studies could be conducted on such mixtures to better characterize possible chemical and physical matrix effects on the C score.

2. *Uncertainties on MOC totals*: With the current version of the quantification models, we observe that points with high SiO_2, FeO and/or MgO content can have high MOC totals (110–120 wt.% for some pure olivine points, discussed in Beyssac et al., 2023). As a consequence, carbonates in mixtures with SiO_2- , FeO- , MgO-rich phases, such as olivine or Fe-Mg pyroxene, may have a relatively high MOC total, so this criterion is not always discriminative.
3. *Ti interferences*: An additional challenge is found in the points enriched in titanium, for two main reasons. First, the database used to train the LIBS quantification models does not include high TiO_2 targets; second, the high density of Ti lines, especially in the UV, results in high degree of overlapping between emission lines of Ti and other elements, which may complicate the characterization of any element's emission (R. B. Anderson et al., 2021). We do not observe a significant correlation of the C score with the Ti signal that could be an indicator of interference, and in particular we observe Ti-rich points with a large range of C scores (−1.9 in Haa_ii_aah #1, sol 109 and 1.83 in Chambares #8, sol 185). Consequently, we do not exclude the Ti-enriched points from our analysis; still, we cannot definitely rule-out the possibility of a bias leading to the over-representation of Ti-rich points among the carbonates detected in the Máaz fm rocks. Additional laboratory analyses of mixtures between Fe-Ti phases and carbonates are required to evaluate the reliability of carbonate detection in Ti-rich points.

4.1.2. Limit of Detection of Carbon in Martian Targets by LIBS

Our C assessment, and the definition of the C score based on the characterization of the C and O LIBS signals, derive from previous studies (e.g., Beck et al., 2017). By measuring a diversity of samples, including mechanical mixtures of carbonate mineral phases and basalts and/or the Martian regolith simulant JSC-1, Beck and collaborators estimated a limit of detection of 13 wt.% of C by this approach. This suggests that only points relatively rich in carbonates can be detected by this approach. Another difficulty is that at this time, we cannot assess the absolute quantity of carbonates in a target and thus we cannot quantify the ratio of cations (e.g., Ca, Fe or Mg) to CO_3. As a result, carbonates belonging to the siderite-magnesite solid solution cannot be discriminated from, for example, pyroaurite $[Mg_6Fe^{3+}_2(CO_3)\,(OH)_{16} \cdot 4H_2O]$, a layered double hydroxide phase with a (Fe + Mg)/CO_3 molar ratio different from siderite-magnesite and forming under significantly different chemical conditions (Zeyen et al., 2019). Similarly, pure Fe-Mg carbonates versus mixtures of Fe-Mg carbonates with Fe- and/or Mg-oxides/hydroxides are difficult to distinguish and can only be inferred approximately by the strength of the C-to-O ratio. Future work using a large reference database, based on mixtures of different carbonate phases mixed with multiple mineral phases, in various proportions, and acquired at different laser-target distances will be crucial for this purpose.

4.1.3. Limits of Detection of Carbonate Phases With IRS and TRR

SuperCam TRR and IR spectroscopies offer two alternatives to LIBS for the detection of carbonates by directly probing vibration modes of the CO_3 functional group. While these spectroscopies have been recognized as particularly relevant for the detection of carbonates, the limits of detection for these mineral phases remain difficult to assess.

With IRS, the depth of the carbonate-related features depend non-linearly on the size of the grains, as well as the mineral phases present in the mixture; target illumination conditions and surface roughness may also affect the depth of the bands, making quantitative assessment extremely challenging. Additionally, overtones and combination bands of carbonates in the shortwave infrared (i.e., at 2.3–2.35 and 2.5–2.55 μm), which are the major bands of carbonates that can be measured by SuperCam, remain relatively weak bands (i.e., low SNR). For example, carbonates in ALH 84001 (1 wt.%) were not detected based on these bands, whereas they were detected

by mid-IR analyses, where fundamental carbonate modes occur (Bishop, Mustard, et al., 1998; Bishop, Pieters, et al., 1998). Moreover, it was repeatedly noticed that the association of clays such as smectites with carbonates, as it might be the case here in Jezero, makes carbonate detection even more difficult because of the overlap of their 2.31-μm band and the resulting reduction of correlation between the 2.3- and 2.5-μm band depths (J. L. Bishop et al., 2013; Horgan et al., 2020; Wray et al., 2016). Furthermore, mixing with opaque grains (e.g., iron rich), especially for small grains, reduces the spectral contrast (depths of the bands); for the relatively weak modes considered here, this may significantly affect the detection capabilities.

Due the short history of Raman analyses on Mars (first time with the Mars 2020 mission) and the specificities of SuperCam remote Raman, limits of detections are not well constrained yet, especially when analyzing samples of varying grain sizes. In general, fine grained samples are inherently difficult to measure with Raman spectroscopy (e.g., Indelicato et al., 2022). Small carbonate grain sizes may therefore explain the relative lack of carbonate detections with SuperCam TRR, and this low signal does not necessarily provide strong constraints on the amount of carbonates present in the analyzed targets. Additionally, iron-rich materials tend to absorb the excitation light, and thus reduce the volume excited by the laser, and hence the resulting Raman signal.

4.1.4. Combination of Techniques

LIBS, TRR and IRS are all consistent about the detection of carbonates in the Garde abraded patch target. However, in several other targets on which all techniques were successively applied, carbonates have clearly been detected by some of the techniques but less confidently or not at all by other techniques. This is probably due to a combination of factors. First, as described in Section 2.1, their analytical footprints are different, varying between for example, 0.35 mm for LIBS and 4.6 mm for IRS for a target at 4 m. This may explain some apparent discrepancies between the techniques, especially if the spatial distribution of carbonates is heterogeneous. Additionally, since LIBS, Raman scattering and reflectance spectroscopy rely on totally different physical processes, these techniques are differently affected by parameters such as grain size, mixtures, dust, distance to the target, temperature and/or target illumination conditions. As a consequence, their limits of detections for a given target are necessarily different. Finally, the detection rate on abraded patches in Seitah (Table S3 Supporting Information S1) is mostly <10%, with all three techniques. Assuming comparable detection rates on natural surfaces, it is improbable to detect carbonate with several techniques on a given target, considering that 9 or 10 points are analyzed on most targets. At the outcrop scale—or on abraded patches—however, we usually perform multiple rasters, which consistently explains why we get more multi-technique detections (e.g., LIBS detection in Nans #9 and IRS detection in Gion #9, both analyzed on sol 242).

4.2. Comparison With Other Detection of Carbonates on Mars

4.2.1. Carbonate Detections With SHERLOC and PIXL in the Crater Floor

Mars2020s proximity science instruments PIXL and SHERLOC (Allwood et al., 2020; Bhartia et al., 2021) also detected carbonates in different target. along the rover traverse (Razzell Hollis et al., 2022; E. L. Scheller et al., 2022; Tice et al., 2022). These detections are consistent with this study and highlight the interesting complementarity of the remote and proximity science instruments, providing fine-scale information on mineral distributions, as well as significant diversity and higher statistics along the traverse of the rover.

Consistent with our results, SHERLOC identified carbonates in the three abraded patches analyzed in the Seitah fm. The carbonate signature detected with SHERLOC in these targets is a carbonate Raman ν_1 mode around 1085 ± 5 cm^{-1}; this is consistent with calcite, but could also match siderite, or some siderite-magnesite solid solutions. These proximity analyses reveal spatial associations of the carbonates with either sulfates or olivines, depending on the target. Through the quantification of major elements, and the co-location with SHERLOC analyses, PIXL also observed carbonates in the Dourbes abraded patch; the team concludes that these are Fe-Mg carbonates, with Fe/Mg of one, comparable to the composition of the olivine grains identified in this target.

SHERLOC also noted some possible (rare and weak) carbonate signatures in two of the four abraded patches analyzed in the Maaz fm. Neither SHERLOC nor PIXL identified any carbonate on the three natural surfaces they analyzed during the crater floor campaign (all three were in the Maaz fm). Even though the spatial distribution of the carbonates detected by SuperCam and SHERLOC in the Maaz formation does not match exactly, the weak

Table 3
Reported Compositions and Amounts of Martian Carbonates From Orbital or In Situ Studies, or Analysis of Martian Meteorites in the Laboratory

Location	Technique/instrument	Carbonate (composition + amount)	Reference
Nili Fossae	Orbital—CRISM on MRO	Mg-rich	(Ehlmann et al., 2008)
		Equal ratio of Fe and Mg	(Brown et al., 2010)
		At a maximum of 20% at the decameter scale	(Edwards & Ehlmann, 2015)
		>9% at the 2–3 km scale	(Salvatore et al., 2018)
		Fe-Mg	(Horgan et al., 2020; Tarnas et al., 2021; Zastrow & Glotch, 2021)
Marginal carbonates in Jezero Crater	Orbital—CRISM on MRO	Hydrated Mg-carbonate	(Horgan et al., 2020)
Syrtis Major, Margaritifer Planum, Lunae Planum, Elysium Planum	Orbital—PSF on Mars Express	Mg-rich, possible small variations of composition between regions	(Palomba et al., 2009)
Comanche outcrop, Columbia Hills, Gusev Crater	In situ—by Spirit (MER)	Mg:Fe of 75:25% 16%–34% of the outcrop	(Morris et al., 2010)
Several craters	Orbital	Ca/Fe carbonates	(Carrozzo et al., 2013; Carter et al., 2015; Wray et al., 2016)
Martian dust	Orbital—TES on Mars Global Surveyor	<5% of carbonates in Martian dust (<10-μm grain size)	(Bandfield, 2003)
Martian equatorial soils	In situ–mini-TES on MER	Mg-carbonates	(Christensen et al., 2004)
Martian Polar soil	In situ—TEGA on Phoenix Polar lander	Calcite, ankerite, dolomite and/or Ca-rich carbonate having a solid solution chemistry with Fe and/or Mg 3-6 wt.%	(Sutter et al., 2012)
in the <150 μm size fraction of soil in Gale crater	In situ—SAM instrument on Curiosity	1%–2% Mg-Fe rich carbonates	(Archer et al., 2014)
Eolian sediments in Gale Crater	In situ—SAM-EGA instrument on Curiosity	~0.7 ± 0.1 wt.% Fe-Mg carbonates	(Sutter et al., 2017)
Glen Torridon, Gale Crater	In situ—CheMin instrument on Curiosity	2.2 wt.% siderite in Kilmarie drill sample Carbonates in 5/7 drill samples	(Bristow et al., 2021; Turner et al., 2022)
Meteorite ALH 84001	Laboratory	Variations from a magnesite endmember, a Fe-Mg endmember and a calcite endmember	(Halevy et al., 2011; Shaheen et al., 2015)
		<1%, heterogeneous distribution	(Bridges et al., 2001; Treiman, 2021)
Nakhlites except Lafayette	Laboratory	Low-Ca, enriched in Fe compared to ALH 84001	(Bridges et al., 2019)
Lafayette	Laboratory	Siderite to calcite	(Bridges et al., 2019)

and rare detections of carbonate in this fm consistently indicate lower carbonate concentration than in Seitah, and a probably more "patchy" distribution of the carbonates, as opposed to their apparent ubiquitousness in Seitah.

4.2.2. Compared Chemical Compositions

The numerous analyses by SuperCam show that the mineralogy of Jezero crater floor is overall dominated by silicates (Beyssac et al., 2023; Udry et al., 2022; Wiens et al., 2022). Yet, SuperCam identified some carbonates, in particular in the patches abraded on Séítah rocks (Garde, Dourbes and Quartier). Here, we compare these carbonates in terms of chemical composition and abundance with past reports of carbonates on Mars, in order to infer possibly related geochemical origins.

As summarized in Table 3, multiple orbital studies characterized carbonate exposures at the surface of Mars, highlighting small variations in chemical composition: reported carbonates are mostly Mg-rich with variable Ca and Fe contents. H_2O absorption bands are also reported in several studies, although it is not clear if these

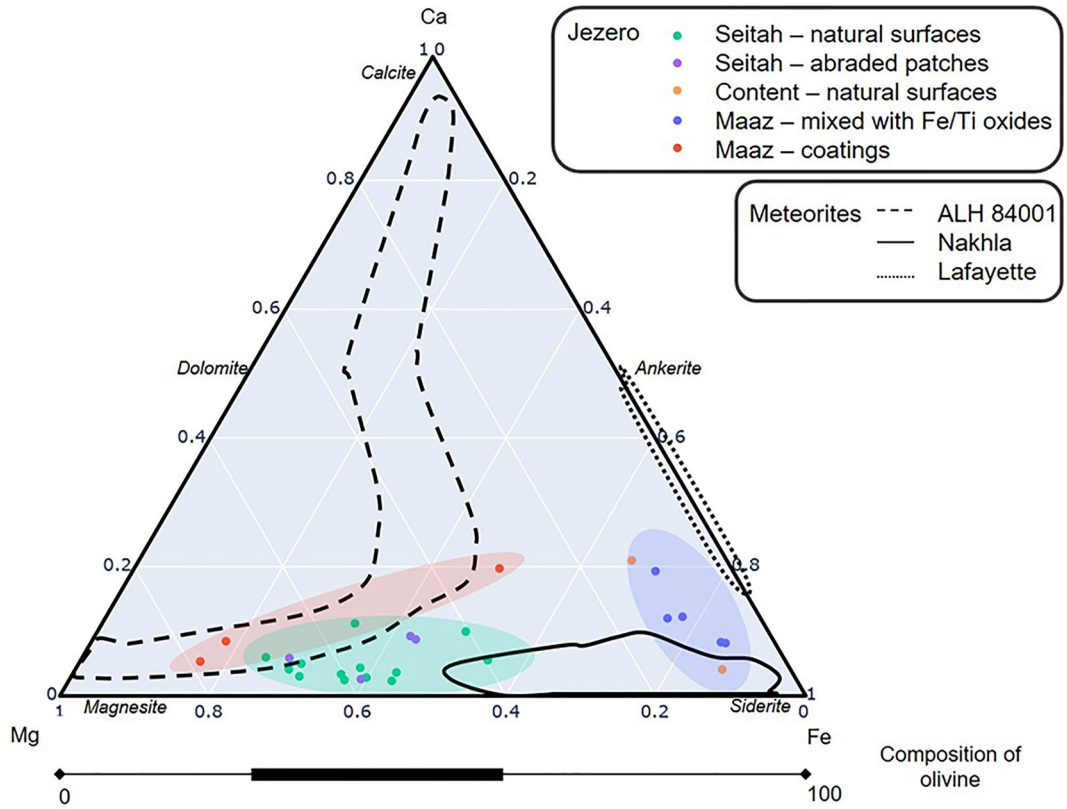

Figure 9. Comparison of the composition of the points where carbonates were detected with laser-induced breakdown spectroscopy in Jezero, to the carbonates found in Martian meteorites (from Bridges et al., 2019), using molar compositions. The bar at the bottom represents the Mg-Fe compositions of the olivines identified in Seitah (in both abraded patches and natural surfaces); no olivine was found in rocks of the Maaz formation or the Content member (Beyssac et al., 2023; Udry et al., 2022).

signatures are related to the carbonates or associated minerals (e.g., Ehlmann et al., 2008). Similar variability is observed in in situ data and in martian meteorites, although the increased spatial resolution results in a more detailed characterization of different carbonates phases. In particular, detailed analyses of carbonates in Martian meteorites showed more complexity, and a significant variability of the composition and spatial distribution of carbonate phases (summarized in Table 3 and shown in Figure 9). In ALH 84001 carbonates are distributed between a magnesite endmember, a Fe-Mg endmember and a calcite endmember (Halevy et al., 2011; Shaheen et al., 2015). The chemical distribution of carbonates in nakhlites seems different with compositions enriched in Fe and poorer in Ca compared to ALH 84001, except in Lafayette where carbonate compositions spread between siderite and calcite (Bridges et al., 2019).

Considering the current accuracy of the MOC, we invite the reader to consider the bulk compositions represented with the colored ellipses in Figure 9, rather than individual data points. We thus observe three main groups, roughly comparable to the Ca-poor parts of the compositions reported in Martian meteorites. Consistent with past orbital observations, most carbonates detected by SuperCam are located in the Séítah fm and are mostly composed of Fe and Mg (green ellipse in Figure 9). LIBS data clearly show that they contain some calcium. Their Ca content is higher than in olivine but remains relatively low, possibly at 2–3 wt.% CaO in general. In any case, no Ca-rich carbonate was detected. Overall, carbonates detected by SuperCam look chemically closest to carbonates reported in nakhlites. LIBS data suggest that they may have a variable Mg#, ranging between 0.42 and 0.70, which is close to the Mg# range covered by olivines detected in Seitah (Beyssac et al., 2023). By contrast, carbonate occurrences in the Máaz formation have different chemical compositions. They are of two kinds. (a) Most are Fe-rich carbonates, that is, siderite (blue ellipse in Figure 9). Detection of siderite in Máaz was inferred from LIBS analyses only, and not confirmed by IRS nor Raman. Siderite was not previously reported from orbit in the Máaz formation. This could be explained by the decrease of sensitivity of IRS and TRR when analyzing

small grained-mixtures, and especially Fe-rich ones, which do not affect LIBS. (b) We also found some probable carbonate coatings, enriched in Mg (Mg# as high as 0.82), spatially associated with sulfates (red ellipse in Figure 9). Interestingly, we observed carbonates in the Content member (orange points inside the blue ellipse in Figure 9) very similar to some detections in the Máaz unit—siderite in Ti-enriched points; this is consistent with previous observations indicating that the Content member is compositionally closest to the Máaz formation, rather than Séítah (Wiens et al., 2022). The detection of siderite spatially associated with a Ti-rich phase, possibly ilmenite, in Content and Maaz is also reminiscent of the observation of siderite-ilmenite assemblages observed in some nakhlites (Bridges & Grady, 1999, 2000).

However, contrary to electron microprobe analyses conducted on carbonate-containing meteorites, SuperCam mostly probes carbonates mixed with another phase and therefore, only provides approximate compositions in this situation, even though our analyses of shot-to-shot trends show that the Ca, Fe and Mg contents of the carbonates and minerals in mixture are generally comparable.

Most carbonates detected by SuperCam were in rock targets, except a few coarse grains in some regolith targets, which are thought to derive from the local bedrock (Table 2). Several studies—based on both orbital and in situ data—reported small amounts (1%–5%) of carbonates in Martian dust or soil (reported in Table 3); the reported compositions vary from Ca-rich, to Mg-rich to Fe-Mg. Considering the low carbonate contents previously estimated in soils, we do not expect to detect them with SuperCam. As stated earlier, due to physical effects of fine-grained textures on spectroscopy analyses, we excluded points analyzed on such materials from our data set and therefore do not report on carbonates in soil or dust.

4.2.3. Compared Abundances

As mentioned in the introduction, the inventory of C at the surface of Mars has been long pursued. Carbonate mineral phases constitute one of the C reservoirs, the size of which needs to be assessed. Previous studies noted that 1% of $CaCO_3$ in the top 500 m of the Martian crust represents the equivalent of a 500 mbar atmospheric reservoir (Manning et al., 2006); this suggests that changes over time in the amount of sequestered carbon may have partly accommodated the variations of the atmospheric reservoir. Moreover, low abundances inferred from surface analyses have been suggested to result from surficial acidic weathering processes, and that carbonates at depth may have not been affected by such loss (Wray et al., 2016). Carbonate amounts reported in previous studies are included in Table 3; we observe a large range of values: from less than 1% in the Martian meteorites to up to 34% in the Comanche outcrop in Gusev Crater.

Here, we do not give a precise quantification of the carbonate content, but try to constrain it: we point out the presence of carbonates in relatively few points (~30/2,000 with LIBS). In these specific points, carbonate content is probably higher than 13 wt.% of C at the scale of LIBS analyses (Beck et al., 2017), but Si emission lines were detected in all points, and the minimal amount of SiO_2 is around 10 wt.% indicating that no pure carbonate was analyzed with averaged LIBS spectra. At the 0.3-mm-scale probed with LIBS, we thus expect carbonate contents between 15% and 80% in the points listed in Table 2. In the IRS data, a quantitative assessment has been performed using nonlinear unmixing based on radiative transfer modeling (Poulet et al., 2022). A mixture of several primary phases (olivine, augite) and secondary phases (phyllosilicate and carbonate) is required for reproducing the spectral signatures of the most promising carbonate-bearing targets in Séítah with up to 10 to 20 vol% of Mg-carbonates estimated for some IRS observations (FOV of a few millimeters) in Dourbes and Garde. At the mm-scale probed with IRS, we observe 3%–20% carbonate in the points listed in Table 1 (i.e., local maximum abundance; consistent with Royer et al., 2022). Overall, the Jezero crater floor is covered with igneous rocks and not carbonate sediments, similarly to the Gusev crater (Squyres et al., 2004). However, our criteria for defining a C-containing point are very conservative and therefore the number of carbonate occurrences is likely underestimated. Second, we may also miss low carbonate abundances such as those previously reported for dust (Bandfield, 2003).

One observation may offer some insight into a comparison between carbonate detection by CRISM versus SuperCam. SuperCam analyzed three targets in Séítah-like rocks at the toe of the current main delta front (mapped as Cf-f2 by Stack et al., 2020), after the drive campaign that took the rover around Séítah (Figure 8b). This location shows signatures characteristic of the regional olivine-carbonate bearing unit from orbit, but previous studies suggested that the carbonate signature is actually stronger there than in the area of Séítah explored during the crater floor campaign (between sol 202 and 342) (Horgan et al., 2020). Consistent with orbital observations,

SuperCam IRS data point toward a higher carbonate concentration in this area than earlier along the rover traverse, and suggests that at least on natural surfaces, detection limits may be similar to CRISM. In particular, one target (Broken_Mountain, analyzed on sol 420) shows some of the deepest carbonate-related features in IRS data (Figure S12 in Supporting Information S1), and it is the only natural-surface target with carbonates detected in more than one point in IRS.

4.3. Implications for Carbonate Formation in the Jezero Crater

Numerous processes have been proposed for the formation of Martian carbonates, including carbonates observed from orbit in Jezero crater (e.g., R. B. Anderson et al., 2021; Bridges et al., 2019; Meslin et al., 2013; Scheller et al., 2021; Tarnas et al., 2021). In this section, we discuss several of these formation processes, and how they may apply to the carbonate phases detected with SuperCam.

The limited abundance of carbonates in the crater floor could be interpreted in different non-exclusive ways: (a) They may have formed with a limited source of CO_2, possibly in subsurface, with no contact with a CO_2-rich atmosphere, favoring the formation of clays over carbonates (Kelemen et al., 2011); (b) They may have formed recently (e.g., in the Amazonian), when the pCO_2 and/or $a(H_2O)$ was low. (c) Trace carbonate abundances may have been further depleted by secondary dissolution and replacement by clays and/or sulfates. (d) Last, the reactivity of the surface of primary minerals such as olivine may have been reduced through a passivation process, limiting carbonation (e.g., Saldi et al., 2015). Hereafter, we discuss in more details some of the formation processes that have been proposed in the past, in light of these new observations.

One type of formation processes involves a relatively recent formation at low water chemical activity and possibly low temperature by rapid olivine carbonation and/or catalysis by heterogeneous electrochemistry (Garenne, 2013; Kelemen, 2020; Shaheen et al., 2010; Wang et al., 2022). Such processes rely on gas-surface interactions and should form carbonates preferentially in the first few micrometers to tens of micrometers at the surface. In Seitah, we did not observe an increased carbonate concentration in surface as opposed to (a) at the depth probed by the last laser shots on a given point (a few micrometers to ~200-μm depth depending on rock hardness) (Chide et al., 2021), or (b) a few millimeters below the surface as analyzed in the abraded patches. Consequently, the distribution of the carbonates we dentified in SuperCam data does not help to confirm or infirm this hypothesis. This may however be consistent with the detection of carbonates only on natural surfaces and not in abraded patches in the Maaz formation. However, it is not clear how these processes occurring in the modern oxidizing atmosphere of Mars may allow the formation of siderite (Fe(II)-containing carbonates) as detected in some Maaz targets. In the Mg-carbonate coatings also observed in Maaz, the Mg-enrichment of the coating with respects to the bulk rock is not consistent with such processes.

A second type of formation processes involves precipitation at relatively low temperature in a saline and/or soda lake (e.g., Ruff et al., 2014). By evaporation, lakes evolve toward a more saline state and become more alkaline, especially in a basaltic watershed, which is eventually conducive to the accumulation of massive carbonate deposits (e.g., Zeyen et al., 2021). Considering that Jezero Crater was shown to contain a lake in the past (Mangold et al., 2021), we must consider this formation process for the carbonates in Jezero. This process was suggested as a possible origin for carbonates in the "Marginal Carbonates" unit, which will be investigated later on in the mission (Horgan et al., 2020). Regarding the carbonates detected on the crater floor, if they were lacustrine in origin, their relatively limited abundance, combined to the low alteration degree of the olivines found in Seitah (Beyssac et al., 2023) would suggest that the lake system was ephemeral as noted for ALH 84001 (Warren, 1998), or that crater floor rocks were rapidly buried under sediments, interrupting alteration. However, in the Máaz and Séítah formations, the detection of Ca-poor, Mg- and Fe-rich carbonates suggests that they may have not precipitated in a lake. Indeed, Ca-carbonates tend to precipitate much faster than Fe-carbonates at low temperature (Jiang & Tosca, 2020) and Mg-uptake within siderite is expected to be limited at low temperature (Sengupta et al., 2020). On Earth, even lacustrine carbonate deposits known to be particularly rich in Mg and composed of, for example, hydromagnesite, such as in Lake Salda (in an ultrabasic geological setting) (Kazanci et al., 2004; Russell et al., 1999) or the extensively studied Lake Alchichica (in a basaltic geological setting) (Zeyen et al., 2019), do contain $CaCO_3$. Therefore, one may expect to detect carbonates with higher Ca content, if they had been formed in a lake. Note that brine infiltration and lake water—groundwater mixing were proposed to explain the detection of siderite associated with what appears to be mixed-layer clay mineral assemblages in Gale crater (Bristow et al., 2021; Thorpe et al., 2022); our observations do not enable us to conclude that this process

may have applied to Jezero, and the igneous rocks found at the floor of Jezero crater are probably less favorable to these processes than more permeable sedimentary deposits. Lastly, the detections of mostly Fe-rich carbonates in the Máaz formation versus (Mg, Fe)-carbonates in the Séítah formation, consistently with the Mg# of these two units, suggest that these carbonates were not formed from the same solution as would be the case in a single lake. Instead, the coincidence of the Mg# of the carbonates and their host rocks for most of our detections indicates probable local alteration of primary minerals at a low water-to-rock ratio.

This is more consistent with the two most favored processes for the formation of most Martian carbonates, involving primary mineral carbonation by either low-temperature fluids such as suggested in ALH 84001 (e.g., Halevy et al., 2011) or hydrothermal fluids (Niles et al., 2013). The circulation of hydrothermal fluids may have been induced by the heat generated by impact events or volcanic activity (Bridges & Schwenzer, 2012; Changela & Bridges, 2010; Crumpler et al., 2020; Daly et al., 2019; Treiman, 2021; Wray et al., 2016). In Jezero, it may have happened shortly after the initial emplacement of the Seitah fm, and in relation with the same magma system, or possibly in relation with the emplacement of the Maaz fm. Moreover, the frequent exposure of carbonates in craters at large scales has been interpreted as the result of excavation of carbonates formed close to the surface before being buried and protected from degradation by late acidic fluids (Wray et al., 2016). Furthermore, the observed heterogeneous distribution of carbonates in the Jezero crater floor (Figure 8, Table S4 in Supporting Information S1), might be consistent with their distribution within cracks, veins or pore spaces through which small amounts of fluids may have circulated.

Additional observations help constrain the formation process of the carbonates. Co-detection of olivine and carbonate from orbit lead to the conclusion that olivine might be the primary phase that is carbonated (Horgan et al., 2020). In situ analyses performed with *Perseverance* in the Séítah formation confirm the association of these two phases: in particular, all the SuperCam IRS and TRR spectra exhibiting carbonate signatures also contain signatures consistent with olivine. Interestingly, in LIBS data, which probe smaller areas than IRS and TRR analyses (a few hundreds of micrometers diameter vs. a few mm), carbonates are not necessarily associated with olivine; in fact, we show that in most cases, carbonates are mixed with Si-rich phases (lower (Fe + Mg)/Si than olivine) enriched in Ca and Na with respects to olivine. This suggests that, at the 0.1-mm scale, a spatial correlation exists between carbonates and phyllosilicates instead of/along with olivine, which is consistent with the association of phyllosilicates with carbonates observed in SuperCam IRS data. This association between carbonates and phyllosilicates has also been noted before by several authors based on orbital measurements or analyses of nakhlites (A. Brown et al., 2021; Bultel et al., 2019; Carrozzo et al., 2017; Dobrea, 2017; Tarnas et al., 2021; Wray et al., 2016). A first conclusion from this observation by Supercam is that the cations composing the phyllosilicates and the carbonate phases (e.g., Al and Ca) in the Seitah formation were not sourced from the olivine only. Instead, fluids precipitating these phases must have also reacted with other phases such as plagioclases, clinopyroxenes or some possible mesostasis. Moreover, the association between phyllosilicates and carbonates may have formed in three ways: (a) These phases formed concomitantly through the alteration of olivine. (b) Carbonates formed by the carbonation of phyllosilicates instead of olivine. Such a process has been shown to be efficient on Earth (Burne et al., 2014) and has been suggested by (Tomkinson et al., 2013) in the Lafayette meteorite based on textural analyses. Smectite would form first by alteration of primary minerals or might be magmatic (Viennet et al., 2020). (c) Carbonates were secondarily replaced by phyllosilicates under conditions that have changed compared to when carbonates formed. Part of the C released upon dissolution of the carbonates may have been transformed to methane as suggested by (Piercy et al., 2022). Analyses of returned samples at high spatial resolution will help to determine whether carbonates replaced phyllosilicates or the other way around.

Regarding the detection of siderite in relatively Ti-enriched targets in both the Content member and Maaz fm, this is consistent with previous observations, in Martian meteorites. Indeed, associations of siderite with ilmenite and magnetite have been observed in some nakhlites (Bridges & Grady, 1999, 2000). Initially, the authors suggested that this may indicate the formation of siderite at elevated temperature in residual melts together with the other interstitial phases (Bridges & Grady, 1999). However, later on, the same authors favored the alternative model involving low temperature crystallization from a brine and interpreting the siderite-ilmenite assemblages as coincidental because both occur in interstitial areas (Bridges & Grady, 2000). Overall, it appears that many observations performed by SuperCam in Jezero are similar to those in nakhlites, notwithstanding their different spatial resolutions.

Finally, Bridges et al. (2019) reported an association between sulfates, halite and carbonates in nakhlites. SuperCam similarly observed such spatial associations in the Jezero crater: carbonates are detected in the Quartier abraded patch, which also contains Mg-sulfates (Meslin et al., 2022); additionally, in the Alk_es_disi target (e.g.,) in the Máaz formation, we observe a salt-bearing coating with compositions different from the rest of the target (Figure 9), especially regarding their MgO content. This is consistent with evaporites, that is, mineral deposits formed by the evaporation of exogenous fluids. Bridges et al. (2019) suggested that carbonates in nakhlites may have formed under hydrothermal conditions and sulfate and halite precipitated upon late evaporation of the hydrothermal fluids. Note, however, that most salts detected in Maaz and Seitah are not associated with the presence of carbonates and they are probably related to different aqueous events.

5. Conclusions

By sol 420, SuperCam has analyzed ∼2,000 points on 220+ targets. Here, using LIBS analyses of major elements as well as C and O, IRS and Raman data, we identified ∼30–40 targets containing carbonate mineral phases. They are mostly found in the Séítah formation, but some were detected in the Máaz formation as well. While these carbonates consist mainly of siderite in the Máaz formation, they belong to the magnesite-siderite solid solution in the Séítah formation (with small amounts of CaO); as a result, the carbonates Mg contents are broadly similar to those of the unit in which they are found. Most carbonate occurrences are associated with phyllosilicates and appear to derive from the local alteration of primary minerals, with a low water-to-rock ratio. A few other carbonate phases are found in coatings and are spatially associated with sulfates; these are the only carbonates we found that showed Mg# significantly different from the rest of the target. They are consistent with evaporites.

By sol 420, Perseverance has collected eight cores. Based on in situ analyses performed with SuperCam in the vicinity of these cores, four of them, acquired in the Seitah formation, may contain carbonate mineral phases. The return of samples to the Earth in ∼2033 offers a unique opportunity to analyze pieces of Mars extracted from a known location and geologic context, with no contaminating terrestrial Ca-carbonates as observed in several Martian meteorites (Bridges et al., 2019). These carbonates may provide critical insights into the petrogenesis of these rocks: First, it will be important to assess the age of carbonates and their hosting minerals for example, by Rb-Sr and Pb-Pb methods (Borg et al., 1999) to contextualize the formation of carbonates in the evolution of Mars surface conditions. Second, it will be important to determine the temperature of carbonate formation as well as the sources of carbon and oxygen based on diverse isotopic measurements to assess the source of C and O (Halevy et al., 2011; Shaheen et al., 2015). Last, textural relationships between phyllosilicates and carbonates should be assessed at high spatial resolution by for example, scanning electron microscopy and/or transmission electron microscopy to determine which phases came first.

Data Availability Statement

The data in this publication are from the SuperCam, MastCam-Z, and WATSON instruments, and the NavCam cameras of the Mars 2020 Perseverance rover. The SuperCam data include the Laser Induced Breakdown Spectroscopy (LIBS), Visible/near infrared (VISIR) Spectroscopy, and the Remote Micro-Imager (RMI). The SuperCam major element oxide composition (MOC), total emissivity, and all raw data and processed calibrated data files are included in the Planetary Data System (Wiens & Maurice, 2021). In addition, all image data presented here from the, and SuperCam and Mastcam-Z instruments are available through the Planetary Data System Imaging Node (https://pds-imaging.jpl.nasa.gov/portal/mars2020_mission.html) and GeoSciences Node (https://pds-geosciences.wustl.edu/missions/mars2020/).

Acknowledgments
We thank the Mars 2020 Science and Engineering teams for their work supporting the scientific research presented in this manuscript. Several contributors are supported by CNES for their work with SuperCam on *Perseverance* (Mars2020). Funding for this work was provided by NASA Mars 2020 Participating Scientist program 80NSSC21K0330 (AU), MICINN, Spain (GLR, MV, KC, JMM; Grant PID2019-107442RB-C31/AEI/10.13039/501100011033), the European Research Council (AGF; Consolidator Grant 818602) and Region Nouvelle-Aquitaine (EC).

References

Algermissen, S., & Padgett, D. (2021). Mars 2020 Rover Mission (M2020) software interface specification—SuperCam instrument experiment data record (EDR) and reduces data records (CDR), data products for non-imaging components. Retrieved from https://pds-geosciences.wustl.edu/m2020/urn-nasa-pds-mars2020_supercam/document/M2020_SuperCam_EDR_RDR_SIS.pdf

Allwood, A. C., Wade, L. A., Foote, M. C., Elam, W. T., Hurowitz, J. A., Battel, S., et al. (2020). PIXL: Planetary instrument for X-ray lithochemistry. *Space Science Reviews*, *216*(8), 134. https://doi.org/10.1007/s11214-020-00767-7

Anderson, D. E., Ehlmann, B. L., Forni, O., Clegg, S. M., Cousin, A., Thomas, N. H., et al. (2017). Characterization of LIBS emission lines for the identification of chlorides, carbonates, and sulfates in salt/basalt mixtures for the application to MSL ChemCam data: LIBS of CL, C, S IN salt-basalt mixtures. *Journal of Geophysical Research: Planets*, *122*(4), 744–770. https://doi.org/10.1002/2016JE005164

Anderson, R. B., Forni, O., Cousin, A., Wiens, R. C., Clegg, S. M., Frydenvang, J., et al. (2021). Post-landing major element quantification using SuperCam laser induced breakdown spectroscopy. *Spectrochimica Acta Part B: Atomic Spectroscopy*, *188*, 106347. https://doi.org/10.1016/j.sab.2021.106347

Archer, P. D., Franz, H. B., Sutter, B., Arevalo, R. D., Coll, P., Eigenbrode, J. L., et al. (2014). Abundances and implications of volatile-bearing species from evolved gas analysis of the Rocknest aeolian deposit, Gale Crater, Mars. *Journal of Geophysical Research: Planets*, *119*(1), 237–254. https://doi.org/10.1002/2013JE004493

Bandfield, J. L., Glotch, T. D., & Christensen, P. R. (2003). Spectroscopic identification of carbonate minerals in the martian dust. *Science*, *301*(5636), 1084–1087. https://doi.org/10.1126/science.1088054

Beck, P., Fau, A., Meslin, P.-Y., Forni, O., & Lasue, J. (2017). Searching for carbon on Mars with MSL ChemCam. *Presented at the LPSC*. Retrieved from https://www.hou.usra.edu/meetings/lpsc2017/pdf/1216.pdf

Benzerara, K., Bernard, S., & Miot, J. (2018). Mineralogical identification of traces of life. In *Biosignatures for Astrobiology*. Springer. https://doi.org/10.1007/978-3-319-96175-0_6

Beyssac, O., Forni, O., Cousin, A., Udry, A., Kah, L.C., Mandon, L., et al. (2023). Petrological traverse of the olivine cumulate Séítah formation at Jezero crater, Mars: A perspective from SuperCam onboard Perseverance. *Journal of Geophysical Research: Planets*, *128*, e2022JE007638. https://doi.org/10.1029/2022JE007638

Bhartia, R., Beegle, L. W., DeFlores, L., Abbey, W., Razzell Hollis, J., Uckert, K., et al. (2021). Perseverance's scanning habitable environments with Raman and luminescence for organics and chemicals (SHERLOC) investigation. *Space Science Reviews*, *217*(4), 58. https://doi.org/10.1007/s11214-021-00812-z

Bibring, J.-P., Langevin, Y., Gendrin, A., Gondet, B., Poulet, F., Berthé, M., et al. (2005). Mars Surface diversity as revealed by the OMEGA/Mars express observations. *Science*, *307*(5715), 1576–1581. https://doi.org/10.1126/science.1108806

Bishop, J. L. (2019). Visible and near-infrared reflectance spectroscopy. In *Remote compositional analysis* (pp. 68–101). Cambridge University Press. https://doi.org/10.1017/9781316888872.006

Bishop, J. L., Mustard, J. F., Pieters, C. M., & Hiroi, T. (1998). Recognition of minor constituents in reflectance spectra of Allan Hills 84001 chips and the importance for remote sensing on Mars. *Meteoritics & Planetary Sciences*, *33*(4), 693–698. https://doi.org/10.1111/j.1945-5100.1998.tb01675.x

Bishop, J. L., Perry, K. A., Darby Dyar, M., Bristow, T. F., Blake, D. F., Brown, A. J., & Peel, S. E. (2013). Coordinated spectral and XRD analyses of magnesite-nontronite-forsterite mixtures and implications for carbonates on Mars: Magnesite-nontronite-forsterite mixtures. *Journal of Geophysical Research: Planets*, *118*(4), 635–650. https://doi.org/10.1002/jgre.20066

Bishop, J. L., Pieters, C. M., Hiroi, T., & Mustard, J. F. (1998). Spectroscopic analysis of Martian meteorite Allan Hills 84001 powder and applications for spectral identification of minerals and other soil components on Mars. *Meteoritics & Planetary Sciences*, *33*(4), 699–707. https://doi.org/10.1111/j.1945-5100.1998.tb01676.x

Borg, L. E., Connelly, J. N., Nyquist, L. E., Shih, C.-Y., Wiesmann, H., & Reese, Y. (1999). The age of the carbonates in martian meteorite ALH84001. *Science*, *286*(5437), 90–94. https://doi.org/10.1126/science.286.5437.90

Bosak, T., Moore, K. R., Gong, J., & Grotzinger, J. P. (2021). Searching for biosignatures in sedimentary rocks from early Earth and Mars (pp. 490–506).

Boynton, W. V., Ming, D. W., Kounaves, S. P., Young, S. M. M., Arvidson, R. E., Hecht, M. H., et al. (2009). Evidence for calcium carbonate at the Mars Phoenix landing site. *Science*, *325*(5936), 61–64. https://doi.org/10.1126/science.1172768

Bridges, J. C., Catling, D. C., Saxton, J. M., Swindle, T. D., Lyon, I. C., & Grady, M. M. (2001). Alteration assemblages in martian meteorites: Implications for near-surface processes (Vol. *28*).

Bridges, J. C., & Grady, M. M. (1999). A halite-siderite-anhydrite-chlorapatite assemblage in Nakhla: Mineralogical evidence for evaporites on Mars. *Meteoritics & Planetary Sciences*, *34*(3), 407–415. https://doi.org/10.1111/j.1945-5100.1999.tb01349.x

Bridges, J. C., & Grady, M. M. (2000). Evaporite mineral assemblages in the nakhlite (martian) meteorites. *Earth and Planetary Science Letters*, *176*(3–4), 267–279. https://doi.org/10.1016/S0012-821X(00)00019-4

Bridges, J. C., Hicks, L. J., & Treiman, A. H. (2019). Carbonates on Mars. In *Volatiles in the martian crust* (pp. 89–118). Elsevier. https://doi.org/10.1016/B978-0-12-804191-8.00005-2

Bridges, J. C., & Schwenzer, S. P. (2012). The nakhlite hydrothermal brine on Mars. *Earth and Planetary Science Letters*, *7*, 117–123. https://doi.org/10.1016/j.epsl.2012.09.044

Bristow, T. F., Grotzinger, J. P., Rampe, E. B., Cuadros, J., Chipera, S. J., Downs, G. W., et al. (2021). Brine-driven destruction of clay minerals in Gale Crater, Mars. *Science*, *373*(6551), 198–204. https://doi.org/10.1126/science.abg5449

Brown, A. J., Goudge, T. A., & Viviano, C. (2021). Mineralogy of Jezero Crater and astrobiological link to Australian Warrawoona group. In *Presented at the 43rd COSPAR scientific assembly. Retrieved from 2021cosp…43E.373B*. Abstract B4.1-0003-21 (oral), id.373.).

Brown, A. J., Hook, S. J., Baldridge, A. M., Crowley, J. K., Bridges, N. T., Thomson, B. J., et al. (2010). Hydrothermal formation of clay-carbonate alteration assemblages in the Nili Fossae region of Mars. *Earth and Planetary Science Letters*, *297*(1–2), 174–182. https://doi.org/10.1016/j.epsl.2010.06.018

Brown, A. J., Viviano, C. E., & Goudge, T. A. (2020). Olivine-carbonate mineralogy of the Jezero Crater region. *Journal of Geophysical Research: Planets*, *125*(3), e2019JE006011. https://doi.org/10.1029/2019JE006011

Bultel, B., Viennet, J.-C., Poulet, F., Carter, J., & Werner, S. C. (2019). Detection of carbonates in martian weathering profiles. *Journal of Geophysical Research*, *19*.

Burne, R. V., Moore, L. S., Christy, A. G., Troitzsch, U., King, P. L., Carnerup, A. M., & Hamilton, P. J. (2014). Stevensite in the modern thrombolites of lake Clifton, Western Australia: A missing link in microbialite mineralization? *Geology*, *42*(7), 575–578. https://doi.org/10.1130/G35484.1

Carrozzo, F. G., Bellucci, G., Altieri, F., & D'Aversa, E. (2013). Detection of carbonate-bearing rocks in craters uplifts of Tyrrhena terra, Mars. In *Presented at the 44th lunar and planetary science conference* (p. 2241).

Carrozzo, F. G., Di Achille, G., Salese, F., Altieri, F., & Bellucci, G. (2017). Geology and mineralogy of the Auki crater, Tyrrhena Terra, Mars: A possible post impact-induced hydrothermal system. *Icarus*, *281*, 228–239. https://doi.org/10.1016/j.icarus.2016.09.001

Carter, J., Loizeau, D., Mangold, N., Poulet, F., & Bibring, J.-P. (2015). Widespread surface weathering on early Mars: A case for a warmer and wetter climate. *Icarus*, *248*, 373–382. https://doi.org/10.1016/j.icarus.2014.11.011

Changela, H. G., & Bridges, J. C. (2010). Alteration assemblages in the nakhlites: Variation with depth on Mars (Vol. *21*).

Chide, B., Lanza, N., Alvarez, C., Angel, S., Bernardi, P., Beyssac, O., et al. (2021). The Supercam microphone to support LIBS investigation on Mars: Review of the first laser-spark recordings (Vol. 4).
Christensen, P. R., Ruff, S. W., Fergason, R. L., Knudson, A. T., Anwar, S., Arvidson, R. E., et al. (2004). Initial results from the mini-TES experiment in Gusev Crater from the Spirit rover. *Science*, *305*(5685), 837–842. https://doi.org/10.1126/science.1100564
Cousin, A., Sautter, V., Fabre, C., Dromart, G., Montagnac, G., Drouet, C., et al. (2022). SuperCam calibration targets on board the perseverance rover: Fabrication and quantitative characterization. *Spectrochimica Acta Part B: Atomic Spectroscopy*, *188*, 106341. https://doi.org/10.1016/j.sab.2021.106341
Crumpler, L. S., Arvidson, R. E., Mittlefehldt, D. W., Grant, J. A., & Farrand, W. H. (2020). Results from the first geologic traverse on the topographic rim of a complex impact crater, Endeavour Crater. *MARS*, *48*(3), 6–257. https://doi.org/10.1130/g46903.1
Daly, L., Lee, M. R., Bagot, P., Halpin, J., Smith, W., McFadzean, S., et al. (2019). Exploring Mars at the nanoscale: Applications of transmission electron microscopy and atom probe tomography in planetary exploration. *Materials Science and Engineering*, *12*.
Dequaire, T., Meslin, P.-Y., Beck, P., Jaber, M., Cousin, A., Rapin, W., et al. (2017). Analysis of carbon and nitrogen signatures with laser-induced breakdown spectroscopy; the quest for organics under Mars-like conditions. *Spectrochimica Acta Part B: Atomic Spectroscopy*, *131*, 8–17. https://doi.org/10.1016/j.sab.2017.02.015
Dobrea, E. Z. N., Niles, P. B., & Cuadros, J. (2017). Ancient hydrothermal seafloor deposits in Eridania basin on Mars. *Nature Communications*, *10*(1), 15978. https://doi.org/10.1038/ncomms15978
Edwards, C. S., & Ehlmann, B. L. (2015). Carbon sequestration on Mars. *Geology*, *43*(10), 863–866. https://doi.org/10.1130/G36983.1
Ehlmann, B. L., Mustard, J. F., Murchie, S. L., Poulet, F., Bishop, J. L., Brown, A. J., et al. (2008). Orbital identification of carbonate-bearing rocks on Mars. *Science*, *322*(5909), 1828–1832. https://doi.org/10.1126/science.1164759
Fairén, A. G. (2010). A cold and wet Mars. *Icarus*, *208*(1), 165–175. https://doi.org/10.1016/j.icarus.2010.01.006
Fairén, A. G., Davila, A. F., Gago-Duport, L., Amils, R., & McKay, C. P. (2009). Stability against freezing of aqueous solutions on early Mars. *Nature*, *459*(7245), 401–404. https://doi.org/10.1038/nature07978
Fairén, A. G., Fernández-Remolar, D., Dohm, J. M., Baker, V. R., & Amils, R. (2004). Inhibition of carbonate synthesis in acidic oceans on early Mars. *Nature*, *431*(7007), 423–426. https://doi.org/10.1038/nature02911
Farley, K. A., Stack, K. M., Shuster, D. L., Horgan, B. H. N., Hurowitz, J. A., Tarnas, J. D., et al. (2022). Aqueously altered igneous rocks sampled on the floor of Jezero crater, Mars. *Science*, *377*(6614), eabo2196. https://doi.org/10.1126/science.abo2196
Farley, K. A., Williford, K. H., Stack, K. M., Bhartia, R., Chen, A., de la Torre, M., et al. (2020). Mars 2020 mission overview. *Space Science Reviews*, *216*(8), 142. https://doi.org/10.1007/s11214-020-00762-y
Farmer, J. D., & Des Marais, D. J. (1999). Exploring for a record of ancient martian life. *Journal of Geophysical Research*, *104*(E11), 26977–26995. https://doi.org/10.1029/1998JE000540
Fouchet, T., Reess, J.-M., Montmessin, F., Hassen-Khodja, R., Nguyen-Tuong, N., Humeau, O., et al. (2022). The SuperCam infrared spectrometer for the perseverance rover of the Mars2020 mission. *Icarus*, *373*, 114773. https://doi.org/10.1016/j.icarus.2021.114773
García-Florentino, C., Torre-Fdez, I., Ruiz-Galende, P., Aramendia, J., Castro, K., Arana, G., et al. (2021). Development of innovative non-destructive analytical strategies for Mars sample return tested on dar al Gani 735 martian meteorite. *Talanta*, *224*, 121863. https://doi.org/10.1016/j.talanta.2020.121863
Garczynski, B. J., Iii, J. F. B., Horgan, B. H. N., Johnson, J. R., Rice, M. S., Vaughan, A., et al. (2022). Perseverance and the purple coating: A Mastcam-Z multispectral story. In *53rd Lunar and Planetary Science Conference*.
Gardiner, D. J., & Graves, P. R. (1989). *Paractical Raman spectroscopy*. Springer-Verlag.
Garenne, A., Montes-Hernandez, G., Beck, P., Schmitt, B., Brissaud, O., & Pommerol, A. (2013). Gas–solid carbonation as a possible source of carbonates in cold planetary environments. *Planetary and Space Science*, *14*, 28–41. https://doi.org/10.1016/j.pss.2012.11.005
Gasnault, O., Mazoyer, J., Cousin, A., Meslin, P.-Y., Lasue, J., Lacour, J.-L., et al. (2012). Deciphering sample and atmosphere oxygen contents with ChemCam on Mars. In *Presented at the 43rd lunar and planetary science conference* (p. 2888).
Golden, D. C., Ming, D. W., Morris, R. V., Brearley, A. J., Lauer, H. V., Jr., Treiman, A. H., et al. (2004). Evidence for exclusively inorganic formation of magnetite in martian meteorite ALH84001. *American Mineralogist*, *89*(5–6), 681–695. https://doi.org/10.2138/am-2004-5-602
Goudge, T. A., Mustard, J. F., Head, J. W., Fassett, C. I., & Wiseman, S. M. (2015). Assessing the mineralogy of the watershed and fan deposits of the Jezero crater paleolake system, Mars: Jezero Paleolake System Mineralogy. *Journal of Geophysical Research: Planets*, *120*(4), 775–808. https://doi.org/10.1002/2014JE004782
Guo, H., He, Q., & Jiang, B. (2008). The application of Mexican Hat wavelet filtering and averaging algorithm in Raman spectra denoising (pp. 321–326). *Presented at the congress on image and signal processing*. https://doi.org/10.1109/CISP.2008.191
Halevy, I., Fischer, W. W., & Eiler, J. M. (2011). Carbonates in the Martian meteorite Allan Hills 84001 formed at 18 ± 4°C in a near-surface aqueous environment. *Proceedings of the National Academy of Sciences*, *108*(41), 16895–16899. https://doi.org/10.1073/pnas.1109444108
Harvey, R. P., & McSween, H. Y. (1996). A possible high-temperature origin for the carbonates in the martian meteorite ALH84001. *Nature*, *382*(6586), 49–51. https://doi.org/10.1038/382049a0
Horgan, B., et al. (2022). Mineralogy, morphology, and geological significance of the Maaz formation and the Jezero crater floor. In *53rd Lunar and Planetary Science Conference* #1680.
Horgan, B. H. N., Anderson, R. B., Dromart, G., Amador, E. S., & Rice, M. S. (2020). The mineral diversity of Jezero Crater: Evidence for possible lacustrine carbonates on Mars. *Icarus*, *339*, 113526. https://doi.org/10.1016/j.icarus.2019.113526
Indelicato, C., Osticioli, I., Agresti, J., Ciofini, D., Mencaglia, A. A., Perotti, M., et al. (2022). Exploring grain sizing of sedimentary calcareous rocks using Raman spectroscopy. In *The European physical journal plus*. https://doi.org/10.1140/epjp/s13360-022-02536-7
International MSR Objectives and Samples Team (iMOST), Beaty, D. W., Grady, M. M., McSween, H. Y., Sefton-Nash, E., Carrier, B. L., et al. (2019). The potential science and engineering value of samples delivered to Earth by Mars sample return. *Meteoritics & Planetary Sciences*, *54*(3), 667–671. https://doi.org/10.1111/maps.13232
Jakosky, B. M., Brain, D., Chaffin, M., Curry, S., Deighan, J., Grebowsky, J., et al. (2018). Loss of the Martian atmosphere to space: Present-day loss rates determined from MAVEN observations and integrated loss through time. *Icarus*, *315*, 146–157. https://doi.org/10.1016/j.icarus.2018.05.030
Jakosky, B. M., & Edwards, C. S. (2018). Inventory of CO_2 available for terraforming Mars. *Nature Astronomy*, *2*(8), 634–639. https://doi.org/10.1038/s41550-018-0529-6
Jiang, C. Z., & Tosca, N. J. (2020). Growth kinetics of siderite at 298.15 K and 1 bar. *Geochimica et Cosmochimica Acta*, *21*, 97–117. https://doi.org/10.1016/j.gca.2020.01.047
Jimenez-Lopez, C., Rodriguez-Navarro, C., Rodriguez-Navarro, A., Perez-Gonzalez, T., Bazylinski, D. A., Lauer, H. V., & Romanek, C. S. (2012). Signatures in magnetites formed by (Ca, Mg, Fe)CO_3 thermal decomposition: Terrestrial and extraterrestrial implications. *Geochimica et Cosmochimica Acta*, *87*, 69–80. https://doi.org/10.1016/j.gca.2012.03.028

Kazanci, N., Girgin, S., & Muzaffer, D. (2004). On the limnology of Salda lake, a large and deep soda lake in southwestern Turkey: Future management proposals (Vol. *12*).

Kelemen, P. B., Matter, J., Streit, E. E., Rudge, J. F., Curry, W. B., & Blusztajn, J. (2011). Rates and mechanisms of mineral carbonation in peridotite: Natural processes and recipes for enhanced, in situ CO_2 capture and storage. *Annual Review of Earth and Planetary Sciences*, *39*(1), 545–576. https://doi.org/10.1146/annurev-earth-092010-152509

Kelemen, P. B., McQueen, N., Wilcox, J., Renforth, P., Dipple, G., & Vankeuren, A. P. (2020). Engineered carbon mineralization in ultramafic rocks for CO_2 removal from air_ Review and new insights. *Chemical Geology*, *22*, 119628. https://doi.org/10.1016/j.chemgeo.2020.119628

Kite, E. S., Gao, P., Goldblatt, C., Mischna, M. A., Mayer, D. P., & Yung, Y. L. (2017). Methane bursts as a trigger for intermittent lake-forming climates on post-Noachian Mars. *Nature Geoscience*, *10*(10), 737–740. https://doi.org/10.1038/ngeo3033

Kite, E. S., Steele, L. J., Mischna, M. A., & Richardson, M. I. (2021). Warm early Mars surface enabled by high-altitude water ice clouds. *Proceedings of the National Academy of Sciences*, *118*(18), e2101959118. https://doi.org/10.1073/pnas.2101959118

Lammer, H., Chassefière, E., Karatekin, Ö., Morschhauser, A., Niles, P. B., Mousis, O., et al. (2013). Outgassing history and escape of the martian atmosphere and water inventory (Vol. *42*).

Lanza, N. L., Ollila, A. M., Cousin, A., Wiens, R. C., Clegg, S., Mangold, N., et al. (2015). Understanding the signature of rock coatings in laser-induced breakdown spectroscopy data. *Icarus*, *249*, 62–73. https://doi.org/10.1016/j.icarus.2014.05.038

Lasue, J., Cousin, A., Meslin, P. Y., Mangold, N., Wiens, R. C., Berger, G., et al. (2018). Martian eolian dust probed by ChemCam. *Geophysical Research Letters*, *45*(20), 10968–10977. https://doi.org/10.1029/2018GL079210

Lasue, J., Meslin, P. Y., Cousin, A., Forni, O., Anderson, R., Beck, P., et al. (2022). Comparison of dust between Gale and Jezero (p. 1758). In *Presented at the 53rd lunar and planetary science conference*.

Legett, C., Newell, R. T., Reyes-Newell, A. L., Nelson, A. E., Bernardi, P., Bender, S. C., et al. (2022). Optical calibration of the SuperCam instrument body unit spectrometers. *Applied Optics*, *61*(11), 2967. https://doi.org/10.1364/AO.447680

Liu, Y., Tice, M. M., Schmidt, M. E., Treiman, A. H., Kizovski, T. V., Hurowitz, J. A., et al. (2022). An olivine cumulate outcrop on the floor of Jezero crater, Mars. *Science*, *377*(6614), 1513–1519. https://doi.org/10.1126/science.abo2756

Madariaga, J. M., Aramendia, J., Arana, G., Castro, K., Gómez-Nubla, L., Fdez-Ortiz de Vallejuelo, S., et al. (2022). Homogeneity assessment of the SuperCam calibration targets onboard rover perseverance. *Analytica Chimica Acta*, *1209*, 339837. https://doi.org/10.1016/j.aca.2022.339837

Mandon, L., et al. (2022). Reflectance of Jezero crater floor: 2. Mineralogical interpretation. *Journal of Geophysical Research: Planets*. https://doi.org/10.1029/2022JE007440

Mandon, L., Quantin-Nataf, C., Thollot, P., Mangold, N., Lozac'h, L., Dromart, G., et al. (2020). Refining the age, emplacement and alteration scenarios of the olivine-rich unit in the Nili Fossae region, Mars. *Icarus*, *336*, 113436. https://doi.org/10.1016/j.icarus.2019.113436

Mangold, N., Gupta, S., Gasnault, O., Dromart, G., Tarnas, J. D., Sholes, S. F., et al. (2021). Perseverance rover reveals an ancient delta-lake system and flood deposits at Jezero Crater, Mars. *Science*, *374*(6568), 711–717. https://doi.org/10.1126/science.abl4051

Manning, C., Mckay, C., & Zahnle, K. (2006). Thick and thin models of the evolution of carbon dioxide on Mars. *Icarus*, *180*(1), 38–59. https://doi.org/10.1016/j.icarus.2005.08.014

Manrique, J. A., Lopez-Reyes, G., Cousin, A., Rull, F., Maurice, S., Wiens, R. C., et al. (2020). SuperCam calibration targets: Design and development. *Space Science Reviews*, *216*(8), 138. https://doi.org/10.1007/s11214-020-00764-w

Maurice, S., Clegg, S. M., Wiens, R. C., Gasnault, O., Rapin, W., Forni, O., et al. (2016). ChemCam activities and discoveries during the nominal mission of the Mars science laboratory in Gale Crater, Mars. *Journal of Analytical Atomic Spectrometry*, *31*(4), 863–889. https://doi.org/10.1039/C5JA00417A

Maurice, S., Wiens, R. C., Bernardi, P., Caïs, P., Robinson, S., Nelson, T., et al. (2021). The SuperCam instrument suite on the Mars 2020 rover: Science objectives and mast-unit description. *Space Science Reviews*, *217*(3), 47. https://doi.org/10.1007/s11214-021-00807-w

Maurice, S., Wiens, R. C., Saccoccio, M., Barraclough, B., Gasnault, O., Forni, O., et al. (2012). The ChemCam instrument suite on the Mars Science Laboratory (MSL) rover: Science objectives and mast unit description. *Space Science Reviews*, *170*(1–4), 95–166. https://doi.org/10.1007/s11214-012-9912-2

Meslin, P.-Y., Forni, O., Beck, P., Cousin, A., Beyssac, O., Lopez-Reyes, G., et al. (2022). Evidence for perchlorate and sulfate salts in Jezero Crater, Mars from SuperCam observations. In *53rd Lunar and Planetrary Science Conference* #2694.

Meslin, P.-Y., Gasnault, O., Forni, O., Schröder, S., Cousin, A., Berger, G., et al. (2013). Soil diversity and hydration as observed by ChemCam at Gale crater, Mars. *Science*, *341*(6153), 1238670. https://doi.org/10.1126/science.1238670

Montagnac, G., Dromart, G., Beck, P., Mercier, F., Reynard, B., Cousin, A., et al. (2018). Spark plasma sintering preparation of reference targets for field spectroscopy on Mars. *Journal of Raman Spectroscopy*, *49*(9), 1419–1425. https://doi.org/10.1002/jrs.5406

Morris, R. V., Ruff, S. W., Gellert, R., Ming, D. W., Arvidson, R. E., Clark, B. C., et al. (2010). Identification of carbonate-rich outcrops on Mars by the Spirit rover. *Science*, *329*(5990), 421–424. https://doi.org/10.1126/science.1189667

Niles, P. B., Catling, D. C., Berger, G., Chassefière, E., Ehlmann, B. L., Michalski, J. R., et al. (2013). Geochemistry of carbonates on Mars: Implications for climate history and nature of aqueous environments. *Space Science Reviews*, *174*(1–4), 301–328. https://doi.org/10.1007/s11214-012-9940-y

Núñez,, J. I., Johnson,, J. R., Horgan,, B. N., Rice,, M. S., Vaughan,, A., Tate,, C., et al. (2022). Stratigraphy and mineralogy ofthe deposits within séítah region on the floor of JEZERO CRATER, mars as seen with MASTCAM-Z (Vol. *2*). LPSC.

Ollila, A. M., Blank, J. G., Wiens, R. C., Lasue, J., Newsom, H. E., Clegg, S. M., et al. (2011). Preliminary results on the capabilities of the ChemCam lase-induced breakdown spectroscopy (LIBS) instrument to detect carbon on Mars. In *Presented at the 42nd lunar and planetary science conference* (p. 2395).

Palomba, E., Zinzi, A., Cloutis, E. A., D'Amore, M., Grassi, D., & Maturilli, A. (2009). Evidence for Mg-rich carbonates on Mars from a 3.9μm absorption feature. *Icarus*, *203*(1), 58–65. https://doi.org/10.1016/j.icarus.2009.04.013

Phillips, R. J., Davis, B. J., Tanaka, K. L., Byrne, S., Mellon, M. T., Putzig, N. E., et al. (2011). Massive CO_2 ice deposits sequestered in the south polar layered deposits of Mars. *Science*, *332*(6031), 838–841. https://doi.org/10.1126/science.1203091

Piercy, J. D., Bridges, J. C., & Hicks, L. J. (2022). Carbonate dissolution and replacement by odinite and saponite in the Lafayette nakhlite: Part of the CO_2-CH_4 cycle on Mars? *Geochimica et Cosmochimica Acta*, *326*, 97–118. https://doi.org/10.1016/j.gca.2022.02.003

Poulet, F., Royer, C., Beck, P., Mandon, L., Quantin-Nataf, C., Johnson, J. R., et al. (2022). Modal mineralogy of Seitah unit in Jezero cater (Mars) retrieved from nonlinear unmixing analyses of IRS/SuperCam (p. 2032). In *Presented at the 53rd lunar and planetary science conference*. Retrieved from https://www.hou.usra.edu/meetings/lpsc2022/pdf/2032.pdf

Ramirez, R. M., & Craddock, R. A. (2018). The geological and climatological case for a warmer and wetter early Mars. *Nature Geoscience*, *11*(4), 230–237. https://doi.org/10.1038/s41561-018-0093-9

Razzell Hollis, J., Moore, K. R., Sharma, S., Beegle, L., Grotzinger, J. P., Allwood, A., et al. (2022). The power of paired proximity science observations: Co-Located data from SHERLOC and PIXL on Mars. *Icarus*, *387*, 115179. https://doi.org/10.1016/j.icarus.2022.115179

Rividi, N., van Zuilen, M., Philippot, P., Ménez, B., Godard, G., & Poidatz, E. (2010). Calibration of carbonate composition using micro-Raman analysis: Application to planetary surface exploration. *Astrobiology*, *10*(3), 293–309. https://doi.org/10.1089/ast.2009.0388

Royer, C., Fouchet, T., Mandon, L., Montmessin, F., Poulet, F., Forni, O., et al. (2022). Reflectance of Jezero crater floor 1. Data processing and calibration of the Infrared Spectrometer (IRS) on SuperCam. *Journal of Geophysical Research: Planets*, *127*, e2022JE007481. https://doi.org/10.1029/2022JE007481

Ruff, S. W., Niles, P. B., Alfano, F., & Clarke, A. B. (2014). Evidence for a Noachian-aged ephemeral lake in Gusev Crater, Mars (Vol. *4*).

Russell, M. J., Ingham, J. K., Zedef, V., Maktav, D., Sunar, F., Hall, A. J., & Fallick, A. E. (1999). Search for signs of ancient life on Mars: Expectations from hydromagnesite microbialites, Salda lake, Turkey. *Journal of the Geological Society*, *156*(5), 869–888. https://doi.org/10.1144/gsjgs.156.5.0869

Saldi, G. D., Daval, D., Guo, H., Guyot, F., Bernard, S., Le Guillou, C., et al. (2015). Mineralogical evolution of Fe–Si-rich layers at the olivine-water interface during carbonation reactions. *American Mineralogist*, *100*(11–12), 2655–2669. https://doi.org/10.2138/am-2015-5340

Salvatore, M. R., Goudge, T. A., Bramble, M. S., Edwards, C. S., Bandfield, J. L., Amador, E. S., et al. (2018). Bulk mineralogy of the NE Syrtis and Jezero crater regions of Mars derived through thermal infrared spectral analyses. *Icarus*, *301*, 76–96. https://doi.org/10.1016/j.icarus.2017.09.019

Scheller, E. L., Razzell Hollis, J., Cardarelli, E. L., Steele, A., Beegle, L. W., Bhartia, R., et al. (2022). Aqueous alteration processes in Jezero Crater, Mars—Implications for organic geochemistry. *Science*, *378*(6624), 1105–1110. https://doi.org/10.1126/science.abo5204

Scheller, E. L., Swindle, C., Grotzinger, J., Barnhart, H., Bhattacharjee, S., Ehlmann, B. L., et al. (2021). Formation of magnesium carbonates on Earth and implications for Mars. *Journal of Geophysical Research: Planets*, *126*(7), e2021JE006828. https://doi.org/10.1029/2021JE006828

Schröder, S., Rammelkamp, K., Vogt, D. S., Gasnault, O., & Hübers, H.-W. (2019). Contribution of a martian atmosphere to laser-induced breakdown spectroscopy (LIBS) data and testing its emission characteristics for normalization applications. *Icarus*, *325*, 1–15. https://doi.org/10.1016/j.icarus.2019.02.017

Sengupta, R., Tosca, N. J., & Robinson, S. A. (2020). Geochemical controls on the elemental composition of siderite: Implications for palaeo-environmental reconstructions. *Geochimica et Cosmochimica Acta*, *271*, 1–15. https://doi.org/10.1016/j.gca.2019.12.010

Shaheen, R., Abramian, A., Horn, J., Dominguez, G., Sullivan, R., & Thiemens, M. H. (2010). Detection of oxygen isotopic anomaly in terrestrial atmospheric carbonates and its implications to Mars. *Proceedings of the National Academy of Sciences*, *107*(47), 20213–20218. https://doi.org/10.1073/pnas.1014399107

Shaheen, R., Niles, P. B., Chong, K., Corrigan, C. M., & Thiemens, M. H. (2015). Carbonate formation events in ALH 84001 trace the evolution of the martian atmosphere. *Proceedings of the National Academy of Sciences*, *112*(2), 336–341. https://doi.org/10.1073/pnas.1315615112

Sharma, S. K., Misra, A. K., Lucey, P. G., Wiens, R. C., & Clegg, S. M. (2007). Combined remote LIBS and Raman spectroscopy at 8.6m of sulfur-containing minerals, and minerals coated with hematite or covered with basaltic dust. *Spectrochimica Acta Part A: Molecular and Biomolecular Spectroscopy*, *68*(4), 1036–1045. https://doi.org/10.1016/j.saa.2007.06.046

Squyres, S. W., Arvidson, R. E., Iii, J. F. B., Bruckner, J., Cabrol, N. A., Calvin, W., et al. (2004). The Spirit rover's Athena science investigation at Gusev Crater, Mars. *Science*, *305*, 7.

Stack, K. M., Williams, N. R., Calef, F., Sun, V. Z., Williford, K. H., Farley, K. A., et al. (2020). Photogeologic map of the perseverance rover field site in Jezero Crater constructed by the Mars 2020 science team. *Space Science Reviews*, *216*(8), 127. https://doi.org/10.1007/s11214-020-00739-x

Sutter, B., Boynton, W. V., Ming, D. W., Niles, P. B., Morris, R. V., Golden, D. C., et al. (2012). The detection of carbonate in the martian soil at the Phoenix landing site: A laboratory investigation and comparison with the thermal and evolved gas analyzer (TEGA) data. *Icarus*, *218*(1), 290–296. https://doi.org/10.1016/j.icarus.2011.12.002

Sutter, B., McAdam, A. C., Mahaffy, P. R., Ming, D. W., Edgett, K. S., Rampe, E. B., et al. (2017). Evolved gas analyses of sedimentary rocks and eolian sediment in Gale crater, Mars: Results of the curiosity rover's sample analysis at Mars instrument from yellowknife Bay to the Namib Dune: SAM-Evolved gas analysis at Gale Crater. *Journal of Geophysical Research: Planets*, *122*(12), 2574–2609. https://doi.org/10.1002/2016JE005225

Tarnas, J. D., Stack, K. M., Parente, M., Koeppel, A. H. D., Mustard, J. F., Moore, K. R., et al. (2021). Characteristics, origins, and biosignature preservation potential of carbonate-bearing rocks within and outside of Jezero Crater. *Journal of Geophysical Research: Planets*, *126*(11). https://doi.org/10.1029/2021JE006898

Thomas-Keprta, K. L., Clemett, S. J., McKay, D. S., Gibson, E. K., & Wentworth, S. J. (2009). Origins of magnetite nanocrystals in martian meteorite ALH84001. *Geochimica et Cosmochimica Acta*, *73*(21), 6631–6677. https://doi.org/10.1016/j.gca.2009.05.064

Thorpe, M. T., Bristow, T. F., Rampe, E. B., Grotzinger, J. P., Fox, V. K., Bennett, K. A., et al. (2021). The mineralogy and sedimentary history of the Glen Torridon region, Gale Crater, Mars (p. 1519). In *Presented at the 52nd lunar and planetary science conference 2021*.

Thorpe, M. T., Bristow, T. F., Rampe, E. B., Tosca, N. J., Grotzinger, J. P., Bennett, K. A., et al. (2022). Mars Science Laboratory CheMin data from the Glen Torridon region and the significance of lake-groundwater interactions in interpreting mineralogy and sedimentary history. *Journal of Geophysical Research: Planets*, *127*(11), e2021JE007099. https://doi.org/10.1029/2021JE007099

Tice, M. M., Hurowitz, J. A., Allwood, A. C., Jones, M. W. M., Orenstein, B. J., Davidoff, S., et al. (2022). Alteration history of Séítah formation rocks inferred by PIXL x-ray fluorescence, x-ray diffraction, and multispectral imaging on Mars. *Science Advances*, *8*(47), eabp9084. https://doi.org/10.1126/sciadv.abp9084

Tomkinson, T., Lee, M. R., Mark, D. F., & Smith, C. L. (2013). Sequestration of martian CO_2 by mineral carbonation. *Nature Communications*, *4*(1), 2662. https://doi.org/10.1038/ncomms3662

Treiman, A. H. (2021). Uninhabitable and potentially habitable environments on Mars: Evidence from meteorite ALH 84001. *Astrobiology*, *21*(8), 940–953. https://doi.org/10.1089/ast.2020.2306

Turner, S. M. R., Schwenzer, S. P., Bridges, J. C., Sutter, B., Thorpe, M. T., Rampe, E. B., & McAdam, A. C. (2022). Carbonate formation in Glen Torridon, Gale Crater, Mars. In *Presented at the 53rd lunar and planetary science conference* (p. 2167). Retrieved from https://www.hou.usra.edu/meetings/lpsc2022/pdf/2167.pdf

Udry, A., Ostwald, A., Sautter, V., Cousin, A., Beyssac, O., Forni, O., et al. (2022). A Mars 2020 Perseverance SuperCam Perspective on the Igneous Nature of the Máaz formation at Jezero crater and link with Séítah, Mars. *Journal of Geophysical Research: Planets*, *127*, e2022JE007440. https://doi.org/10.1029/2022JE007440

Valley, J. W., Eiler, J. M., Graham, C. M., Gibson, E. K., Romanek, C. S., & Stolper, E. M. (1997). Low-temperature carbonate concretions in the martian meteorite ALH84001: Evidence from stable isotopes and mineralogy. *Science*, *275*(5306), 1633–1638. https://doi.org/10.1126/science.275.5306.1633

Viennet, J.-C., Bernard, S., Le Guillou, C., Sautter, V., Schmitt-Kopplin, P., Beyssac, O., et al. (2020). Tardi-magmatic precipitation of Martian Fe/Mg-rich clay minerals via igneous differentiation. *Geochemical Perspectives Letters*, 47–52. https://doi.org/10.7185/geochemlet.2023

Viviano-Beck, C. E., Seelos, F. P., Murchie, S. L., Kahn, E. G., Seelos, K. D., Taylor, H. W., et al. (2014). Revised CRISM spectral parameters and summary products based on the currently detected mineral diversity on Mars. *Journal of Geophysical Research: Planets*, *119*(6), 1403–1431. https://doi.org/10.1002/2014JE004627

Wang, A., Yan, Y., Houghton, J., Jolliff, B., Jackson, A., Sturchio, N., et al. (2022). Martian carbonates generated by atmosphere-surface interaction. In *Presented at the 53rd lunar and planetary science conference*.1116

Warren, P. H. (1998). Petrologic evidence for low-temperature, possibly flood evaporitic origin of carbonates in the ALH84001 meteorite.

Wiens, R. C., & Maurice, S. (2021). Mars 2020 SuperCam bundle. In *NASA planetary data system*. https://doi.org/10.17189/1522646

Wiens, R. C., Maurice, S., Barraclough, B., Saccoccio, M., Barkley, W. C., Bell, J. F., et al. (2012). The ChemCam instrument suite on the Mars Science Laboratory (MSL) rover: Body unit and combined system Tests. *Space Science Reviews*, *170*(1–4), 167–227. https://doi.org/10.1007/s11214-012-9902-4

Wiens, R. C., Maurice, S., Robinson, S. H., Nelson, A. E., Cais, P., Bernardi, P., et al. (2021). The SuperCam instrument suite on the NASA Mars 2020 rover: Body unit and combined system Tests. *Space Science Reviews*, *217*(1), 4. https://doi.org/10.1007/s11214-020-00777-5

Wiens, R. C., Udry, A., Beyssac, O., Quantin-Nataf, C., Mangold, N., Cousin, A., et al. (2022). Compositionally and density stratified igneous terrain in Jezero Crater, Mars. *Science Advances*, *8*(34), eabo3399. https://doi.org/10.1126/sciadv.abo3399

Wordsworth, R., Ehlmann, B., Forget, F., Haberle, R., Head, J., & Kerber, L. (2018). Healthy debate on early Mars. *Nature Geoscience*, *11*(12), 888. https://doi.org/10.1038/s41561-018-0267-5

Wray, J. J., Murchie, S. L., Bishop, J. L., Ehlmann, B. L., Milliken, R. E., Wilhelm, M. B., et al. (2016). Orbital evidence for more widespread carbonate-bearing rocks on Mars: More widespread carbonate rocks on Mars. *Journal of Geophysical Research: Planets*, *121*(4), 652–677. https://doi.org/10.1002/2015JE004972

Zastrow, A. M., & Glotch, T. D. (2021). Distinct carbonate lithologies in Jezero Crater, Mars. *Geophysical Research Letters*, *48*(9). https://doi.org/10.1029/2020GL092365

Zent, A. P., & Quinn, R. C. (1995). Simultaneous adsorption of CO_2 and H_2O under Mars-like conditions and application to the evolution of the Martian climate. *Journal of Geophysical Research*, *100*(E3), 5341. https://doi.org/10.1029/94JE01899

Zeyen, N., Benzerara, K., Beyssac, O., Daval, D., Muller, E., Thomazo, C., et al. (2021). Integrative analysis of the mineralogical and chemical composition of modern microbialites from ten Mexican lakes: What do we learn about their formation? (p. 140).

Zeyen, N., Benzerara, K., Menguy, N., Brest, J., Templeton, A. S., Webb, S. M., et al. (2019). Fe-bearing phases in modern lacustrine microbialites from Mexico. *Geochimica et Cosmochimica Acta*, *253*, 201–230. https://doi.org/10.1016/j.gca.2019.03.021